NAVAL POSTGRADUATE SCHOOL

MONTEREY, CALIFORNIA

THESIS

SAR IMAGE FORMATION WITH EMBEDDED QPSK COMMUNICATIONS IN LFM GUARDBANDS AND UAV ANTENNA CHARACTERIZATION

by

Mariano Negron Perez

March 2022

Thesis Advisor: Ric Romero
Co-Advisor: David C. Jenn

Approved for public release. Distribution is unlimited.

THIS PAGE INTENTIONALLY LEFT BLANK

REPORT DOCUMENTATION PAGE	*Form Approved OMB No. 0704-0188*

1. AGENCY USE ONLY *(Leave blank)*	**2. REPORT DATE** March 2022	**3. REPORT TYPE AND DATES COVERED** Master's thesis

4. TITLE AND SUBTITLE SAR IMAGE FORMATION WITH EMBEDDED QPSK COMMUNICATIONS IN LFM GUARDBANDS AND UAV ANTENNA CHARACTERIZATION	**5. FUNDING NUMBERS** RE336
6. AUTHOR(S) Mariano Negron Perez	
7. PERFORMING ORGANIZATION NAME(S) AND ADDRESS(ES) Naval Postgraduate School Monterey, CA 93943-5000	**8. PERFORMING ORGANIZATION REPORT NUMBER**
9. SPONSORING / MONITORING AGENCY NAME(S) AND ADDRESS(ES) SAF	**10. SPONSORING / MONITORING AGENCY REPORT NUMBER**

11. SUPPLEMENTARY NOTES The views expressed in this thesis are those of the author and do not reflect the official policy or position of the Department of Defense or the U.S. Government.

12a. DISTRIBUTION / AVAILABILITY STATEMENT Approved for public release. Distribution is unlimited.	**12b. DISTRIBUTION CODE** A

13. ABSTRACT (maximum 200 words)

Synthetic aperture radar (SAR) imaging with the use of a small-sized unmanned aerial vehicle (UAV) is a fairly recent and very promising application. There are two main thrusts in this thesis: a) SAR imaging with radar-communications waveform, and b) antenna characterizations with a UAV. Quadrature phase shift keying (QPSK) modulation is embedded to transmit data to a communications receiver via the guardbands of a linear frequency modulated (LFM) signal for SAR. Images are formed with the LFM-QPSK combined signal (i.e., there is no need to filter out the communications signal in the radar receiver). We vary signal-to-noise power ratio and LFM to communications bandwidth ratio and investigate how each parameter affects the SAR images generated. We also look at the effect of shifting the communications carriers away from the LFM spectrum on the SAR image. The next step in developing and fielding a system is selecting an antenna and performing a pattern characterization with a UAV via radio frequency transmission to ground receiver. Antenna characterization is performed by transmitting a continuous wave signal from a UAV and measuring received power from a seven-element Yagi antenna on the ground.

14. SUBJECT TERMS unmanned aerial vehicle, UAV, SAR, radar, embedded QPSK, linear frequency modulated, LFM	**15. NUMBER OF PAGES** 97
	16. PRICE CODE

17. SECURITY CLASSIFICATION OF REPORT	**18. SECURITY CLASSIFICATION OF THIS PAGE**	**19. SECURITY CLASSIFICATION OF ABSTRACT**	**20. LIMITATION OF ABSTRACT**
Unclassified	Unclassified	Unclassified	UU

NSN 7540-01-280-5500

Standard Form 298 (Rev. 2-89)
Prescribed by ANSI Std. 239-18

THIS PAGE INTENTIONALLY LEFT BLANK

Approved for public release. Distribution is unlimited.

SAR IMAGE FORMATION WITH EMBEDDED QPSK COMMUNICATIONS IN LFM GUARDBANDS AND UAV ANTENNA CHARACTERIZATION

Mariano Negron Perez
Lieutenant, United States Navy
BS, North Carolina State University, 2013

Submitted in partial fulfillment of the
requirements for the degree of

MASTER OF SCIENCE IN ELECTRICAL ENGINEERING

from the

NAVAL POSTGRADUATE SCHOOL
March 2022

Approved by: Ric Romero
Advisor

David C. Jenn
Co-Advisor

Douglas J. Fouts
Chair, Department of Electrical and Computer Engineering

THIS PAGE INTENTIONALLY LEFT BLANK

ABSTRACT

Synthetic aperture radar (SAR) imaging with the use of a small-sized unmanned aerial vehicle (UAV) is a fairly recent and very promising application. There are two main thrusts in this thesis: a) SAR imaging with radar-communications waveform, and b) antenna characterizations with a UAV. Quadrature phase shift keying (QPSK) modulation is embedded to transmit data to a communications receiver via the guardbands of a linear frequency modulated (LFM) signal for SAR. Images are formed with the LFM-QPSK combined signal (i.e., there is no need to filter out the communications signal in the radar receiver). We vary signal-to-noise power ratio and LFM to communications bandwidth ratio and investigate how each parameter affects the SAR images generated. We also look at the effect of shifting the communications carriers away from the LFM spectrum on the SAR image. The next step in developing and fielding a system is selecting an antenna and performing a pattern characterization with a UAV via radio frequency transmission to ground receiver. Antenna characterization is performed by transmitting a continuous wave signal from a UAV and measuring received power from a seven-element Yagi antenna on the ground.

THIS PAGE INTENTIONALLY LEFT BLANK

Table of Contents

List of Figures

THIS PAGE INTENTIONALLY LEFT BLANK

List of Tables

THIS PAGE INTENTIONALLY LEFT BLANK

List of Acronyms and Abbreviations

CLBR	Comms-to-LFM bandwidth ratio
CW	Continuous wave
LCBR	LFM-to-communications bandwidth ratio
LFM	Linear frequency modulated
MLD	Maximum likelihood detection
NPS	Naval Postgraduate School
QPSK	Quadrature phase shift keying
RCR	Radar power-to-communications power ratio
RF	Radio frequency
SAR	Synthetic aperture radar
SNR	Signal-to-noise power ratio
UAS	Unmanned aircraft system
UHF	Ultrahigh frequency

THIS PAGE INTENTIONALLY LEFT BLANK

Acknowledgments

First, I want to thank my wife, Alexira Rodriguez, and my kids, Yeymari and Junjun. Thank you for supporting me and pushing me to be a better person each day. Thank you to my mom, dad, brothers and sisters, for always being there for me.

Thank you to my advisor, Ric Romero, laboratory technician Manuel Badiola, co-advisor David Jenn, technical problem sponsor Dr. Pat Ford and ECE Naval Postgraduate School for their contribution to this work.

Last but not least, special thanks to associate Jann C. Rohde and three NPS graduates: Madjer de Andrade Martins, Konstantinos Paschalidis and Monica Lavris. Without you, this might not have been possible. Thank you.

THIS PAGE INTENTIONALLY LEFT BLANK

CHAPTER 1:
Introduction

Radar has advanced significantly since becoming a critical technology in World War II. Synthetic aperture radars (SARs) are widely used by military and civilian organizations in topography, oceanography and navigation. Their remote sensing and mapping capabilities can be used in almost any weather condition, and of course, day and/or night. Linear frequency modulation (LFM) is a common SAR waveform because it offers a very fine range resolution capability by using a high bandwidth.

The idea in this work is for a radar to illuminate a target area from a drone-mounted SAR, form a SAR image, and at the same time, transmit data to a communications receiver on the ground. Drones and other types of unmanned aircraft vehicles (UAVs) are used in many applications such as: aerial photography, videography, communications, crop spraying, intelligence gathering, surveillance targeting, and now even as radar platforms. In 1937, the United States Navy developed the Curtiss-N2C-2 drone, which was one of the first radio-controlled aircraft. During World War II, the Germans developed the V-1 Doodlebug, a UAV fitted with explosives and a pulsejet. The V-1 was used for the terror bombing of London. Recent research has utilized UAVs in RF applications. In 2019, the authors in [1] propose utilizing drones as relay nodes to receive, demodulate, and retransmit signals to a final receiver for demodulation and beamforming. The work in [2] attempts to characterize air-to-ground wireless communications between UAV platforms and users on the ground both in practical line of sight and non line of sight scenarios across a wide range of carrier frequencies, including cellular and Wi-Fi (5 GHz) frequency bands. The authors in [3] propose the development of a lightweight, multimode, ultra-high frequency, ultra-wideband radar module. The proposed design is for drone-based operation, and is therefore, low-weight, compact, and easy to maintain. It features low power consumption and a drone-independent power supply.

Also growing is the field of radar-communications spectral sharing, in which radar-embedded communications is a very good example. SAR fundamentals and signal processing algorithms are well covered in several books such as [4]. Both [5] and [6] provide

excellent exposure into the topic of spectral sharing. Indeed, a quick search will produce many recent works, but they cannot all be added here for brevity. Several cited works explore ways to improve radar and data communications while considering cooperation between both as a joint system instead of being mutually exclusive. The work in [7] explores the RF spectrum congestion problem and provides possible options to increase efficiency and optimize spectrum use. The work in [8] explores utilizing intrapulse radar-embedded communication signals for covert communications. The works in [9] and [10] investigate the radar-communications spectral sharing problem and propose ways to improve the performance of both systems. The work in [11] explores demodulation of QPSK radar-embedded communications using least squares estimator and maximum likelihood detection (MLD) while [12] compares deep neural network machine learning demodulation with the MLD method.

For example, in [13], quaternary phase-shift keying (QPSK) carriers are placed in the radar guardbands. This modulation provides a decent combination of spectral efficiency and symbol error rate performance. Typically, communications signals require less power than radar signals due to one-way link propagation. As such, radar power-to-communications power ratio (RCR) is large in most cases. However, this thesis focuses on taking advantage of the guardbands. We allow two communications signals be adjacent to the LFM waveform and use the combined return signal to generate the SAR picture. The base SAR MATLAB code utilized in this work is from "Fundamentals of Radar Signal Processing" by M. Richards [14]. That code is expanded in this research.

1.1 Objectives

The idea in this work is for a radar to illuminate a target area from a drone-mounted SAR, form a SAR image, and at the same time, transmit data to a communications receiver on the ground. The communications receiver may or may not be in the target area, as illustrated in Figure 1.1. The communications receiver is a focal point in [13]. This thesis focuses on the radar receiver.

To realize a SAR-imaging drone system, several aspects have to be studied, but we only focus on two. The objectives are: a) to simulate a comms-radar waveform and produce a SAR image, and b) to characterize the performance of a potential antenna to be used on

a drone. In Chapters 2 through 4, we investigate if an embedded communications signal degrades or improves SAR image formation. In Chapters 5 and 6, we conduct experiments with a UAV to transmit a RF signal to a ground receiver for characterization of potential antenna candidates.

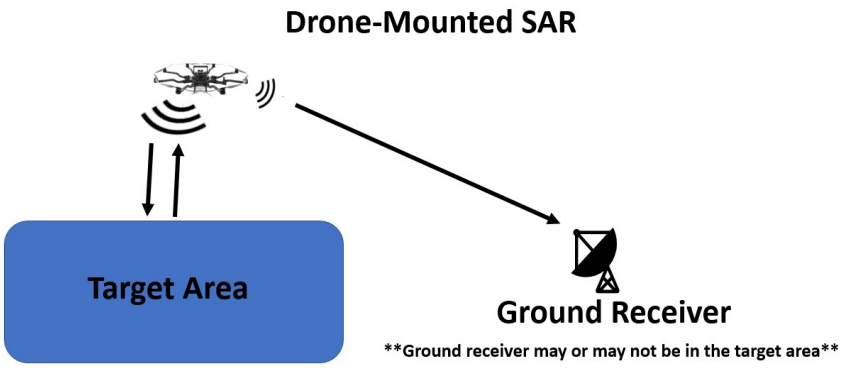

Figure 1.1. Drone-mounted SAR communications illustration

THIS PAGE INTENTIONALLY LEFT BLANK

CHAPTER 2:
Signal Modeling for SAR and Communications

Communications links are normally one-way paths (i.e., transmitter to receiver). Monostatic radar typically travels a two-way path, since the backscatter (reflected combined signal) needs to be processed at the radar receiver. The radar probability of detection is barely affected by modulating the transmitted signal with a communications signal, as long as the RCR remains high. This thesis investigates generating the SAR picture without filtering out the communications signal.

As stated before, the goal is to place QPSK carriers in the guardbands of an LFM pulse and investigate their effect on the SAR picture generated by the radar. In Figure 2.1, we illustrate the 5 us, 15 MHz bandwidth LFM pulse utilized in this work, with some noise to give a 30 dB signal-to-noise power ratio (SNR). In Figure 2.2, the corresponding SAR image using nine targets is illustrated. This work uses Figure 2.2 as a baseline to compare succeeding results in which QPSK signals have been added in the guardbands.

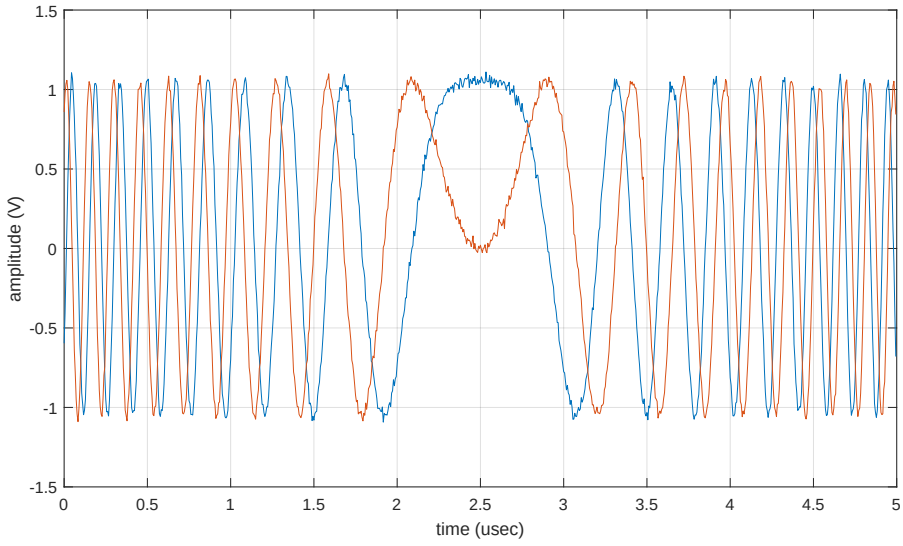

Figure 2.1. Baseline LFM waveform with a 15 MHz bandwidth, 30 dB SNR, and no communications added

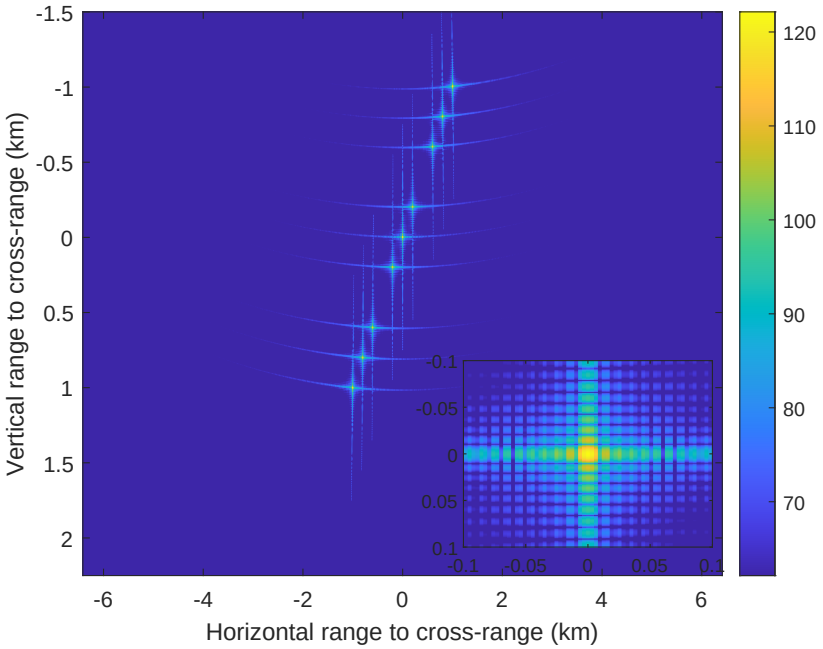

Figure 2.2. SAR picture generated from baseline LFM waveform and corresponding color bar [dB], 30 dB SNR, no embedded communication signal

2.1 Baseband Signal Description, Normalized Sampling Time

For the time being, we assume the signal is complex baseband, with normalized sampling time. The noise-free transmitted and eventually received complex baseband signal is modeled in the form $x[n] = r[n] + c[n]$, where n is the time index, $r[n]$ is the radar LFM signal, and $c[n] = c_1[n] + c_2[n]$ is the sum of the two QPSK communications signals that are added on the left and right side of the LFM mainlobe respectively. Let f_1 and f_2 be the carrier frequencies of the communications signals, and $\phi[n]$ the QPSK phase sequence in which the possible values is from the set $\{\pi/4, 3\pi/4, 5\pi/4, 7\pi/4\}$. The two QPSK signals are given by:

$$\begin{aligned} c_1[n] &= Ae^{j(2\pi f_1 n)} e^{j\phi_1[n]} \\ c_2[n] &= Ae^{j(2\pi f_2 n)} e^{j\phi_2[n]}, \end{aligned} \tag{2.1}$$

where A is the amplitude. Assuming thermal noise in the receiver, the received signal plus noise is $y[n] = r[n] + c[n] + w[n]$, where $w[n]$ is zero-mean additive white Gaussian noise of variance σ^2 for $n = 0, 1, 2, \ldots, N-1$ (where N is the number of samples). Note that in SAR, clutter is ever present and a more complicated received signal modeling is absolutely needed for practical scenarios, but that is beyond the scope of this thesis. More research is required to expand the received signal model as mentioned in Section 7.1.

Modern communications signals also use pulse shaping filters for both spectrum efficiency and inter-symbol interference (ISI) mitigation. Thus, another interesting research aspect is to add the effect of pulse-shaping filter into SAR imaging parameters. These are beyond the scope of this thesis, but it is proposed to look into these interesting practical waveform aspects in the future.

2.1.1 Practical bandwidths and carrier frequencies

For SAR image generation, it is best to use practical bandwidths instead of bandwidths less than normalized frequency (or normalized sampling time which is sometimes a convenient model). Using actual bandwidth allows a practical feel for the temporal/range resolution offered by the LFM waveform. Let t_s = 5.55 nsec be the sampling time, and W = 15 MHz be the bandwidth as in the utilized base code [14]. Then, let F_1 and F_2 be the carrier frequencies for the communications signals. The carrier frequencies may be shifted towards or away from the LFM mainlobe (still centered at 0 Hz) as desired using the LFM bandwidth as a reference. The expressions for the subcarrier frequencies are given by:

$$\begin{aligned} F_1 &= -W/2 - (f_\Delta W) \\ F_2 &= W/2 + (f_\Delta W), \end{aligned} \tag{2.2}$$

where the carriers are shifted in relation to the LFM cutoff (3 dB) bandwidth by $f_\Delta W$. In other words, if f_Δ is allowed to be 1, then F_1 is -1.5W. This left carrier frequency is exactly one bandwidth frequency interval away from the LFM left hand 3 dB point.

Although not advisable, in both equations, if f_Δ is negative, then the QPSK center frequencies f_1 and f_2 are shifted toward the LFM signal mainlobe. When f_Δ is positive, the QPSK center frequencies are shifted away from the LFM mainlobe. This thesis proposes f_Δ not be less than 0, since that will put the subcarrier frequencies inside the mainlobe (which defeats

the idea of utilizing guardbands for communications). In reality, even if the subcarrier is outside the mainlobe, there will be spectral overlap between the LFM waveform and the communications waveform depending on the pulse shape of the QPSK symbol. In this work, no pulse-shaping filter is used, but it is proposed to investigate such topic in Chapter 7 of this thesis. The symbol rate for the QPSK modulation is given by $R_s = 1/T_{sym}$. If C is the number of QPSK symbols in radar pulse τ, then it should be clear that $T_{sym} = \tau/C$. In other words, this means the symbol rate is $R_s = C/\tau$, per subcarrier. Since there are two subcarriers, the total $R_t = 2R_s$.

Notice that the spectral overlap between the LFM mainlobe and the QPSK can be significant depending on the radar-to-communications bandwidth ratio or LFM-comms bandwidth ratio (LCBR) which is given by:

$$LCBR = W/R_s. \tag{2.3}$$

The effective LCBR_e is LCBR/2. The reciprocal is defined as the comms-to-LFM bandwidth ratio (CLBR).

A sample spectrum of a combined LFM-QPSK signal is shown in Figure 2.3. In this example, $f_\Delta = 0$, $F_1 = -W/2$ and $F_2 = W/2$. In other words, the subcarrier frequencies are at the LFM cutoff frequencies. Recall that the LFM signal alone has a bandwidth of 15 MHz. Also in Figure 2.3, a case where $C = 900$ symbols is displayed, which means that LCBR is 0.0833. The same number of QPSK symbols is added per subcarrier, which means both subcarriers have the same communications bandwidth. Note that the QPSK center frequencies F_1 and F_2 are equidistant from the origin (center frequency of the LFM which is 0 Hz here). As R_s increases, so does the LFM-communications overlap. The two subcarrier spectra overlap also increases. In other words, care must be employed to increase R_s. This work varies R_s and f_Δ to see the effect on SAR image formation.

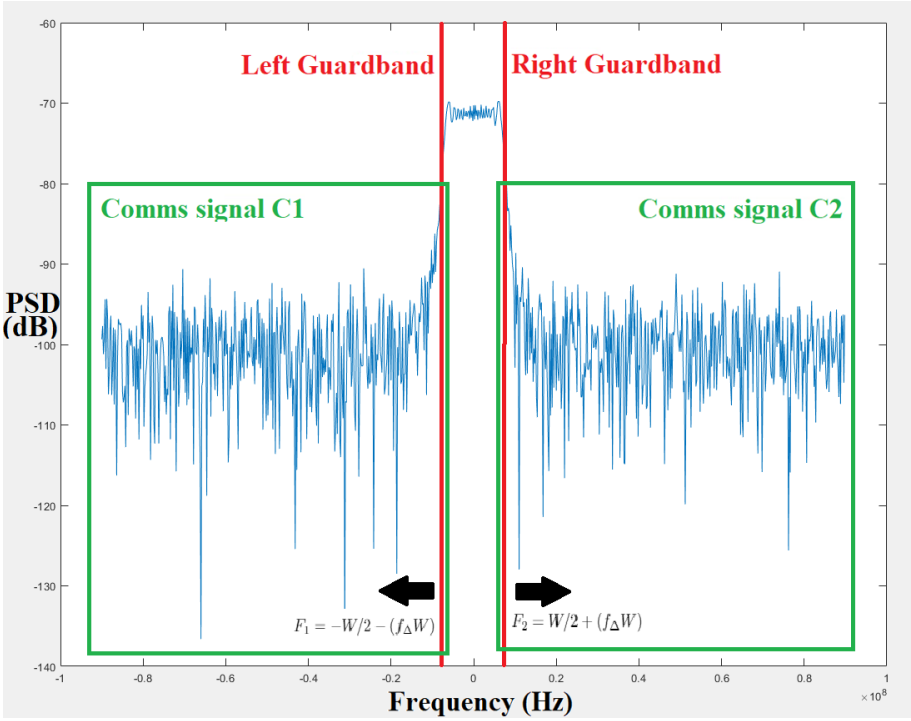

Figure 2.3. RF spectrum of LFM waveform with 900 symbols per QPSK subcarrier. LCBR = 0.0833. No noise, 20dB RCR, $f_\Delta = 0$

2.2 Constants and Variables

In this section, the constants and variables listed in Table 2.1 are defined. These are utilized for analysis and simulations in future sections. Let N be the number of samples in the LFM waveform; τ is the pulse length; f_s is the sampling frequency; the sampling time t_s is the reciprocal of f_s; W is the LFM signal bandwidth; azimuth/range resolution is minimum distance between two targets in order for the radar to distinguish between them; otherwise, they appear to be one single target; R_{crp} is the range to swath center; v is the aircraft/platform speed; f_c is the RF frequency; D_{az} is the antenna azimuth size; and L_s is the swath length (diameter). Some of the parameters assigned in [14] are retained purely for convenient illustration in this work.

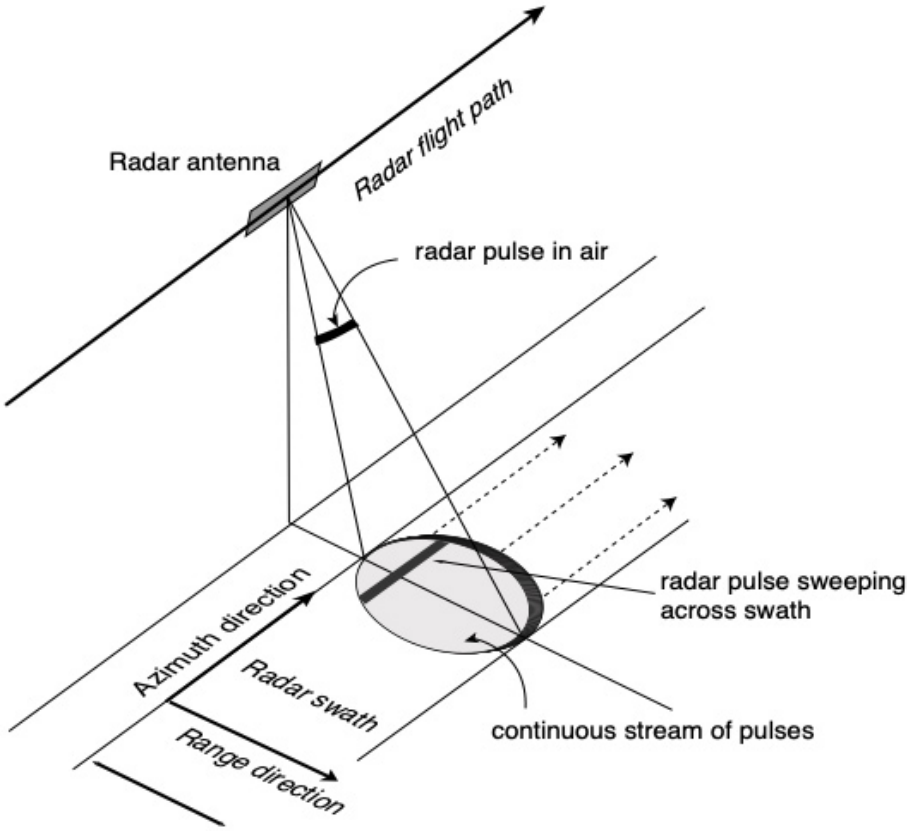

Figure 2.4. SAR illustration. Source: [15].

Table 2.1. Constants and variables utilized in simulation

Variable	Value	Units
N	900	samples
τ	5	μsec
f_s	180	MHz
t_s	5.55	nsec
W	15	MHz
Azimuth/range resolution	10	meters
R_{crp}	30000	meters
v	150	m/s
f_c	1e10	Hz
D_{az}	0.2	meters
L_s	3000	meters

CHAPTER 3:
Processing

In our simulation scenario, nine targets are placed in a diagonal line. The actual positions in meters are defined in Table 3.1. The SAR images are formed using the range Doppler algorithm from [14], which is modified to include the communications subcarriers signal. SAR images are generated by parameterizing one variable of interest at a time.

Table 3.1. Actual position of simulation targets (meters)

Target	X	Y
1	-1000	1000
2	-800	800
3	-600	600
4	-200	200
5	0	0
6	1000	-1000
7	800	-800
8	600	-600
9	200	-200

In Figure 3.1, the effects of increasing the number of QPSK symbols in one LFM waveform pulse are displayed. In this example, $f_\Delta = 0.25$, SNR is 30 dB, and RCR is 20 dB. The time domain waveforms for the combined LFM-QPSK signals are shown for: (a) no communications, (b) 9 symbols per subcarrier, (c) 90 symbols per subcarrier, and (d) 900 symbols per subcarrier. Typical radar systems transmit constant amplitude waveforms for transmit amplifier efficiency. While the resulting combined waveform may not be of constant amplitude (as shown in Figures 3.1 and 3.2), it may be close, especially at high RCR.

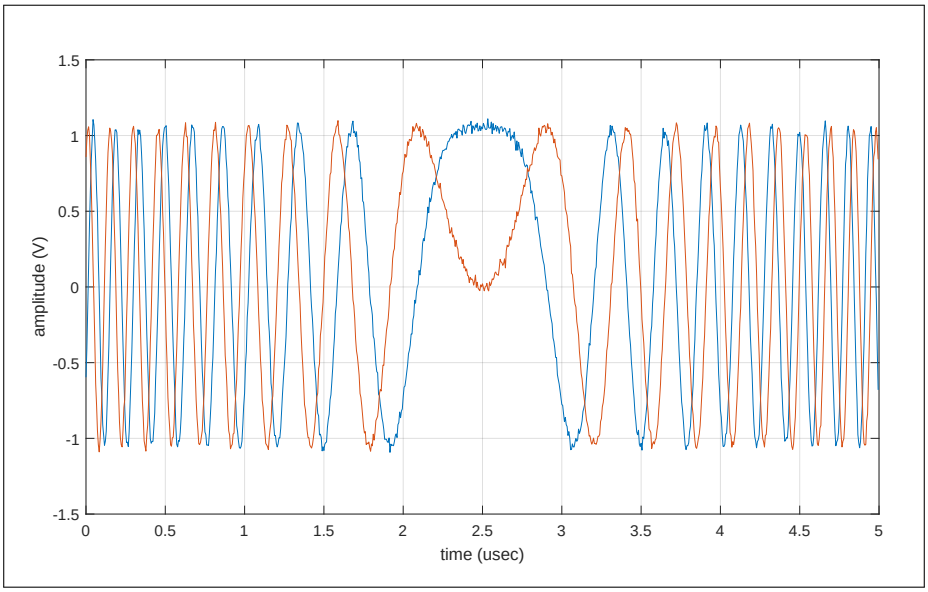

(a)

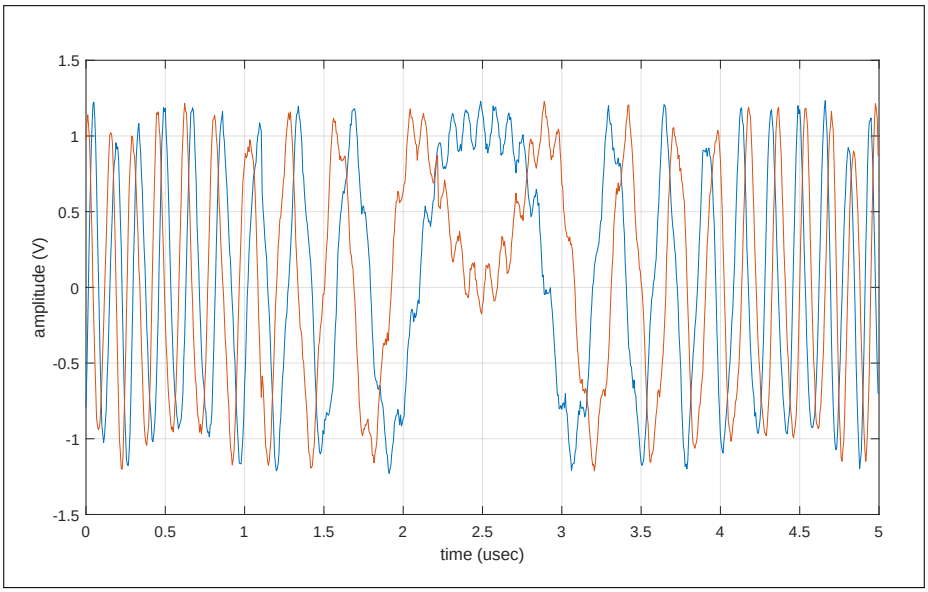

(b)

Figure 3.1. LFM waveform with SNR = 30 dB, RCR = 20 dB, $f_\Delta = 0.25$, (a) no communication baseline (top), (b) 9 symbols (bottom), (c) 90 symbols, and (d) 900 symbols (continued on next page)

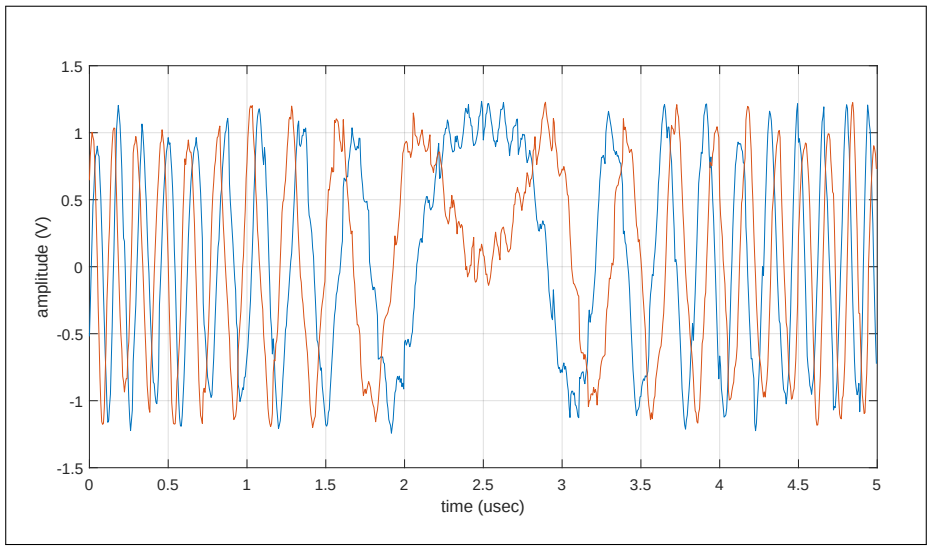

(c)

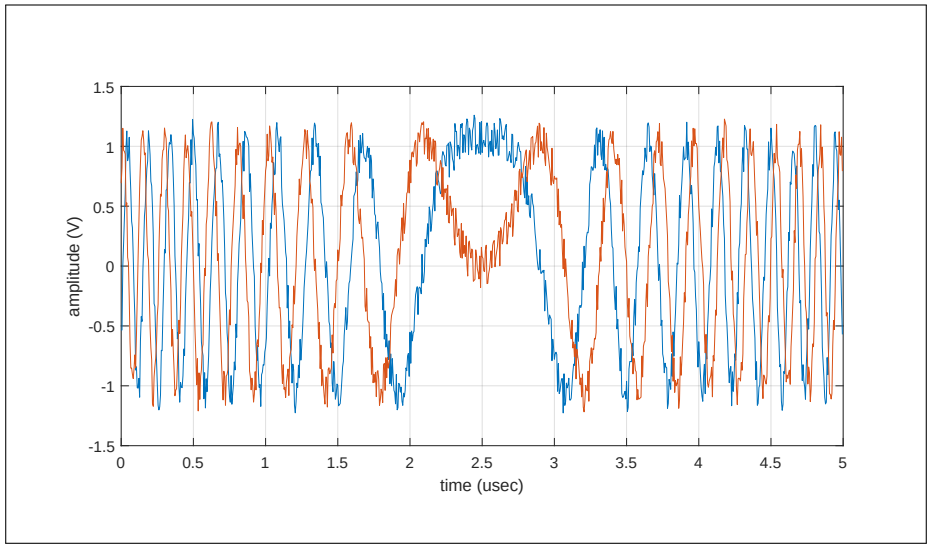

(d)

Figure 3.1. (continued from previous page) LFM waveform with SNR = 30 dB, RCR = 20 dB, $f_\Delta = 0.25$, (a) no communication baseline, (b) 9 symbols, (c) 90 symbols (top), and (d) 900 symbols (bottom)

Another example is displayed in Figure 3.2. In this case $f_\Delta = 0.50$. All other parameters remain the same as in Figure 3.1. The effects of increasing the number of QPSK symbols in one LFM waveform pulse are again evident. The time domain waveforms for the combined

LFM-QPSK signals are shown for: (a) no communications, (b) 9 symbols per subcarrier, (c) 90 symbols per subcarrier, and (d) 900 symbols per subcarrier.

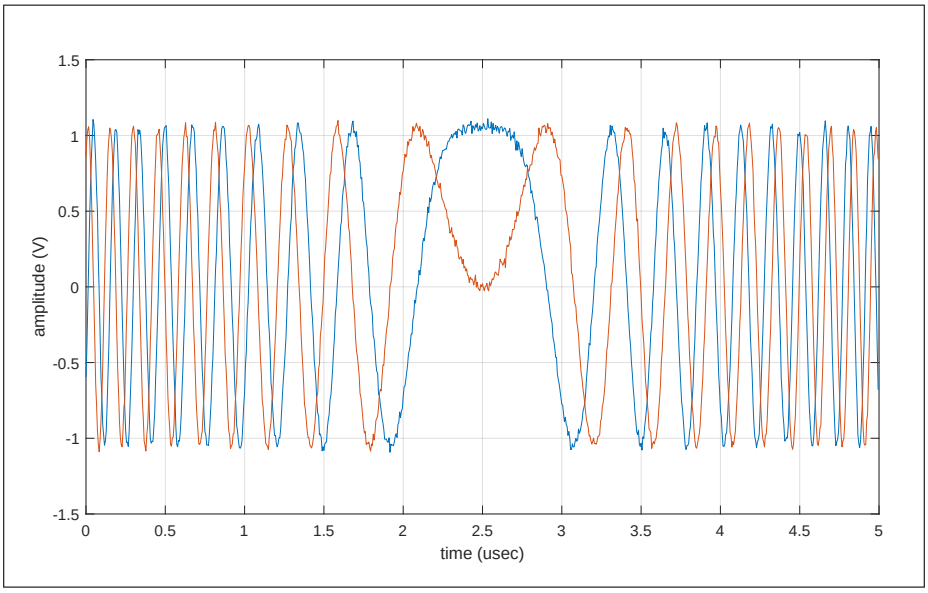

(a)

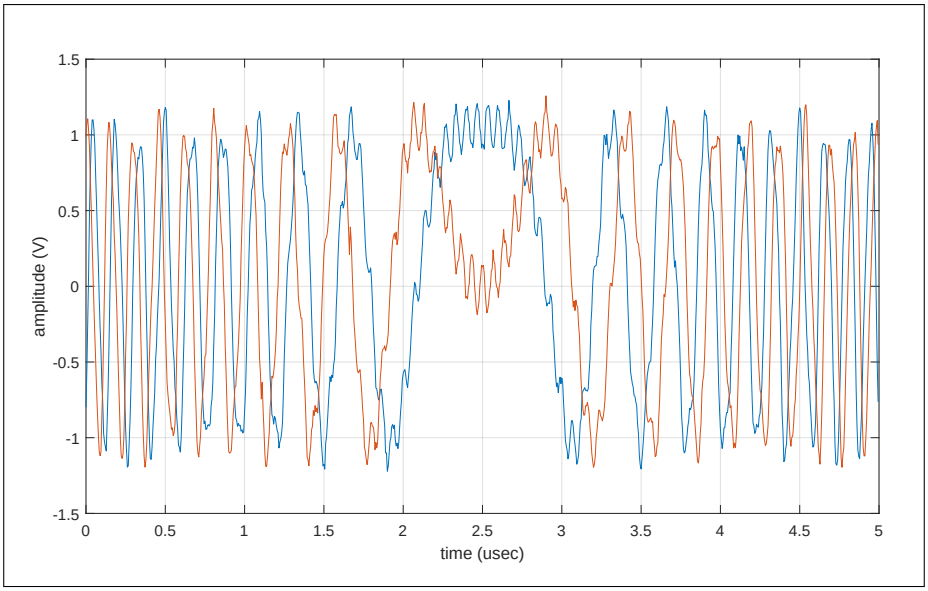

(b)

Figure 3.2. LFM waveform with SNR = 30 dB, RCR = 20 dB, $f_\Delta = 0.5$, (a) no communication baseline (top), (b) 9 symbols (bottom), (c) 90 symbols, and (d) 900 symbols (continued on next page)

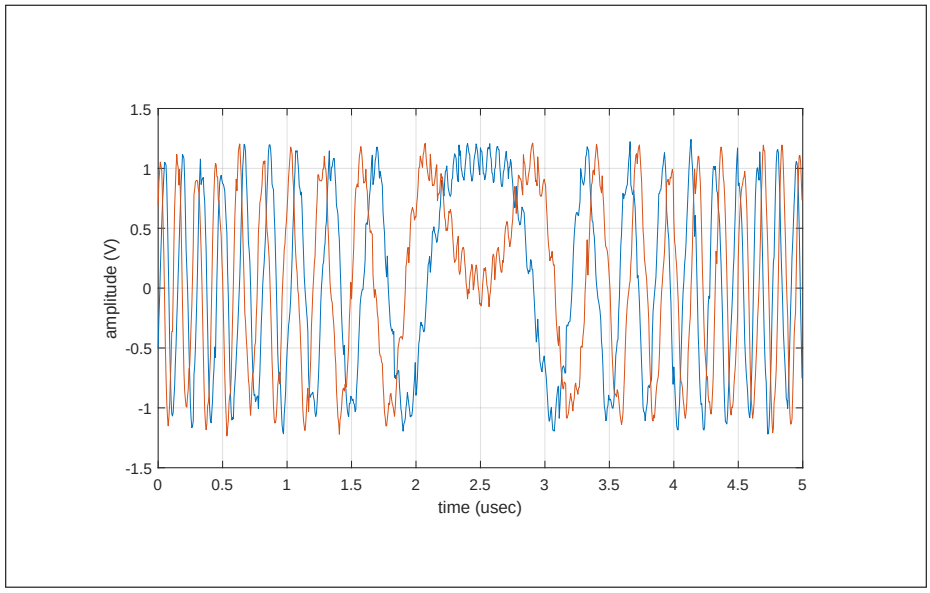

(c)

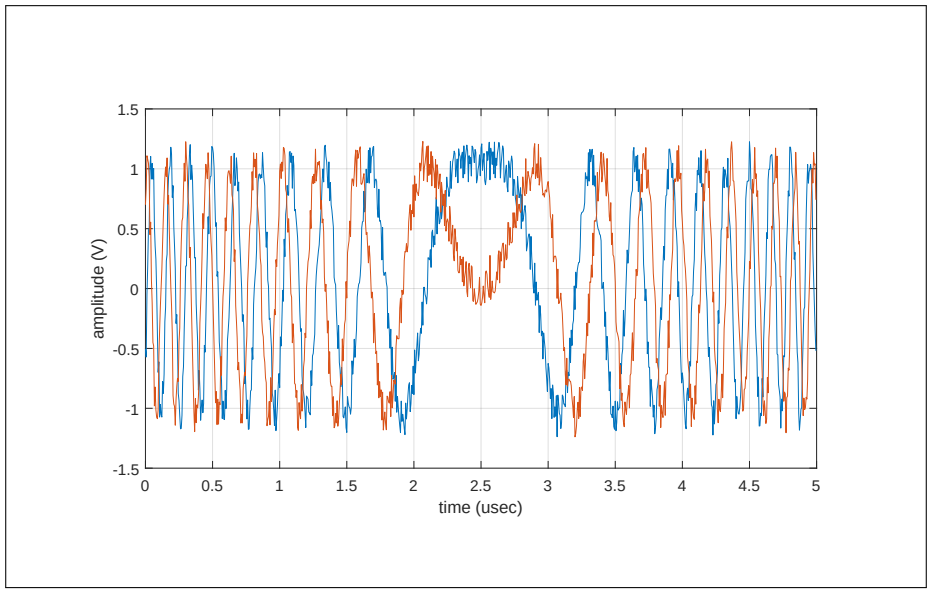

(d)

Figure 3.2. (continued from previous page) LFM waveform with SNR = 30 dB, RCR = 20 dB, $f_\Delta = 0.5$, (a) no communication baseline, (b) 9 symbols, (c) 90 symbols (top), and (d) 900 symbols (bottom)

The corresponding spectra from Figures 3.1 and 3.2 are illustrated in Figures 3.3 and 3.4, respectively. Note the case of 900 symbols per subcarrier, which corresponds to an LCBR of 0.0833 or CLBR of 12. To increase the total bandwidth of the combined signal, one must increase the number of symbols. Notice that CLBR = 12 (900 symbols) accomplishes that. In theory, this may yield better resolution if the combined signal is used to process the return signal. Note, however, that if the guardband frequency interval is constrained, then a CLBR = 12 may not necessarily be allowed. The use of 90 symbols per subcarrier, which corresponds to CLBR = 1.2, may be more reasonable. Unfortunately, due to the high RCR, communications spectrum is low compared to the LFM spectrum. In other words, the effective bandwidth increase may not be discernable in the SAR image anyway. Regardless, our goal is: a) see if the communications signal actually degrades the SAR image in some fashion, and b) see if there is a discernable improvement in range resolution in terms of the SAR images.

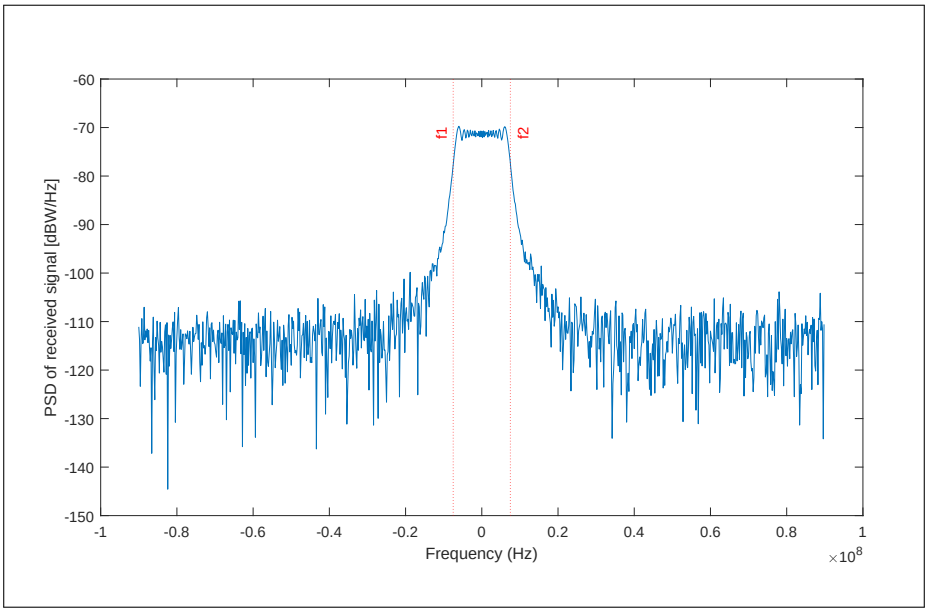

(a)

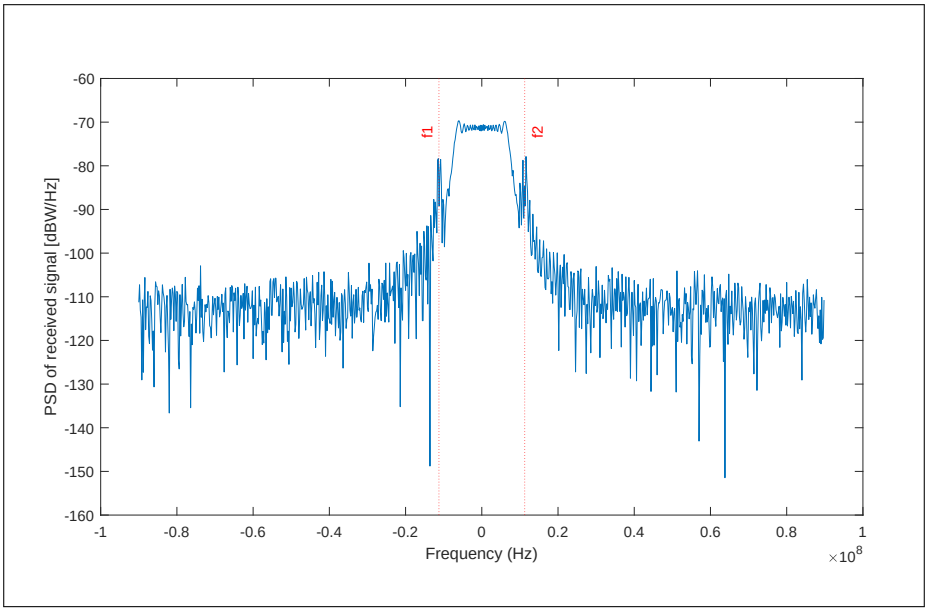

(b)

Figure 3.3. PSD of backscatter signal SNR = 30 dB, RCR = 20 dB, f_Δ = 0.25, (a) no communication baseline (top), (b) 9 symbols per subcarrier (bottom), (c) 90 symbols per subcarrier, and (d) 900 symbols per subcarrier (continued on next page)

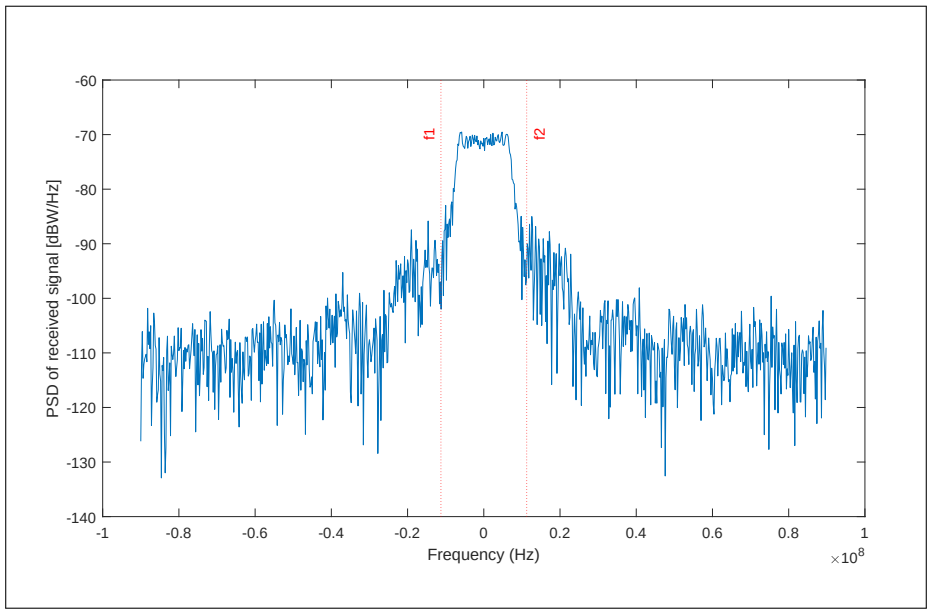

(c)

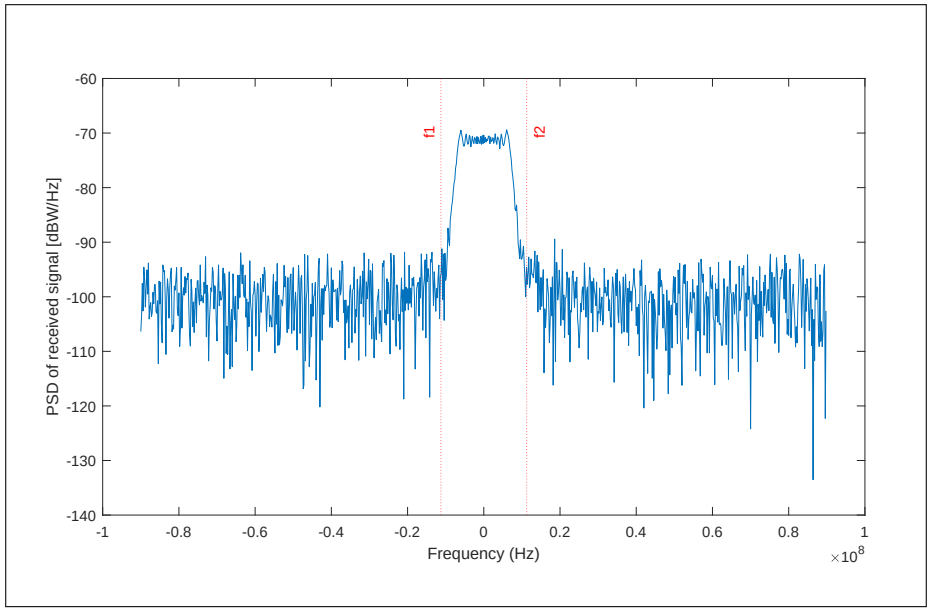

(d)

Figure 3.3. (continued from previous page) PSD of backscatter signal SNR = 30 dB, RCR = 20 dB, f_Δ = 0.25, (a) no communication baseline, (b) 9 symbols per subcarrier, (c) 90 symbols per subcarrier (top), and (d) 900 symbols per subcarrier (bottom)

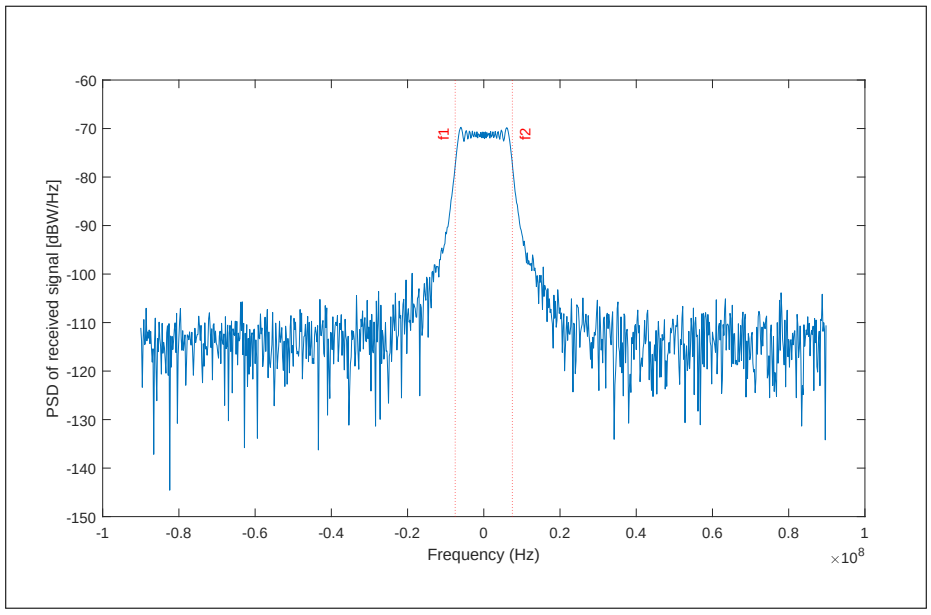

(a)

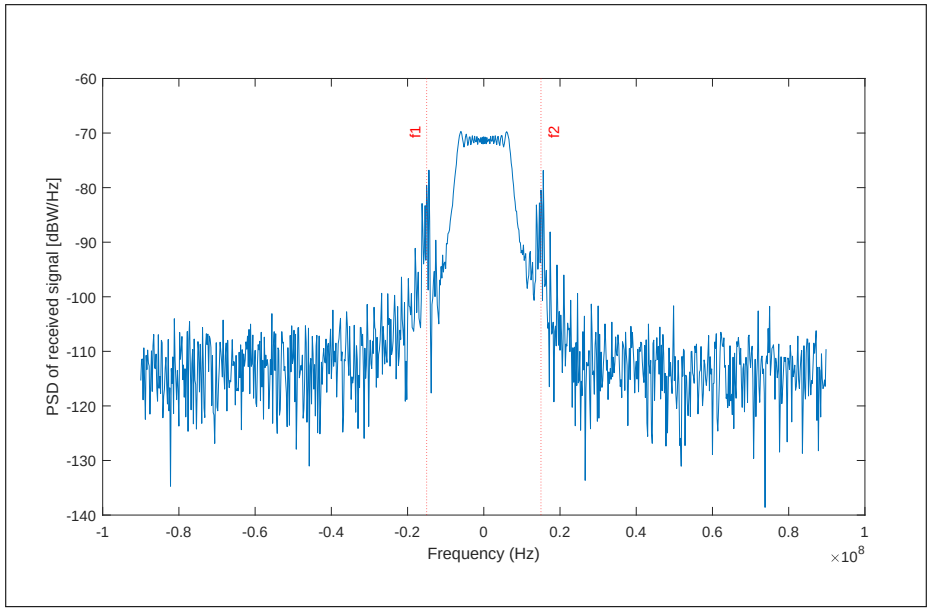

(b)

Figure 3.4. PSD of backscatter signal SNR = 30 dB, RCR = 20 dB, f_Δ = 0.50, (a) no communication baseline (top), (b) 9 symbols per subcarrier (bottom), (c) 90 symbols per subcarrier, and (d) 900 symbols per subcarrier (continued on next page)

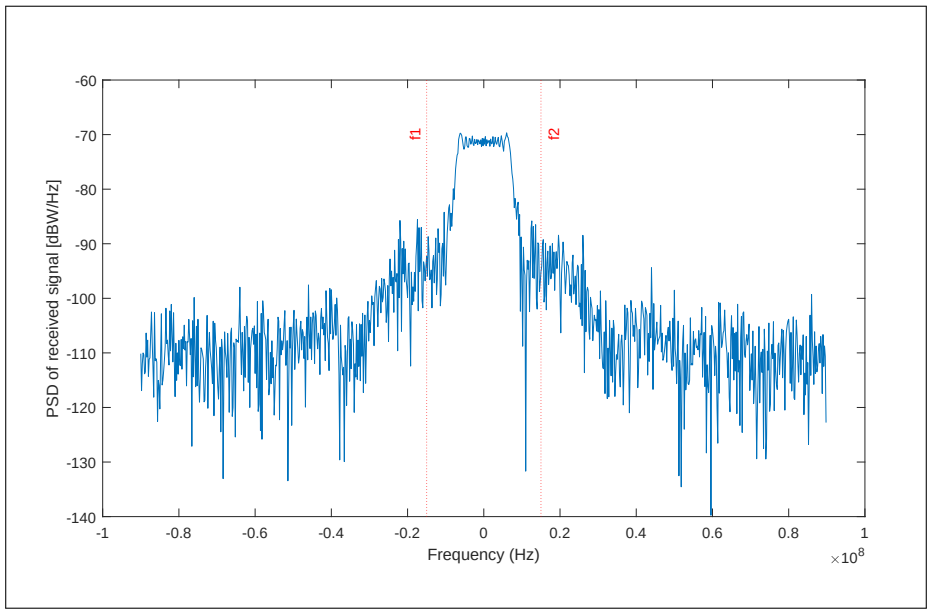

(c)

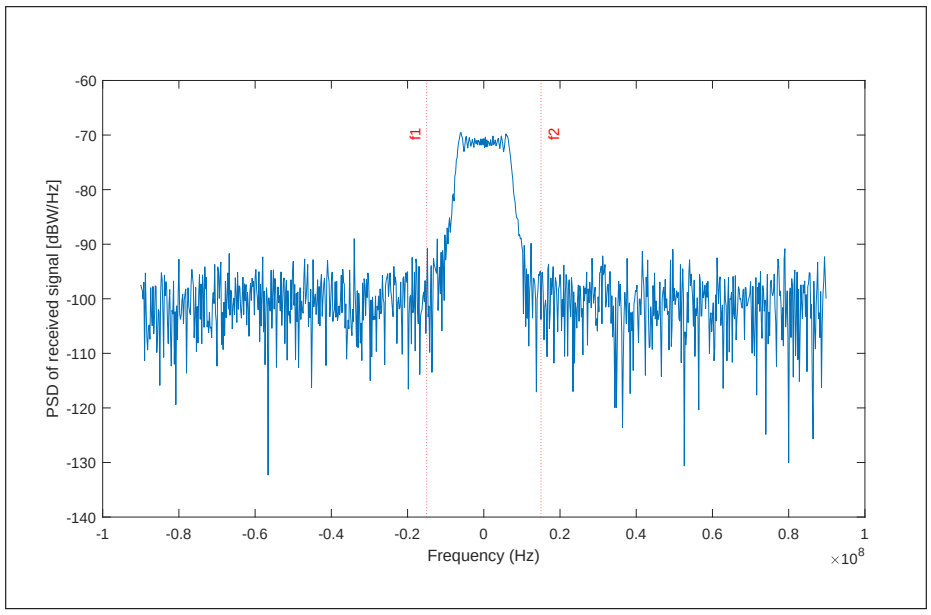

(d)

Figure 3.4. (continued from previous page) PSD of backscatter signal SNR = 30 dB, RCR = 20 dB, f_Δ = 0.50, (a) no communication baseline, (b) 9 symbols per subcarrier, (c) 90 symbols per subcarrier (top), and (d) 900 symbols per subcarrier (bottom)

CHAPTER 4:
Simulation Results

Figure 4.1 shows the SAR images produced utilizing SNR = 30 dB, RCR = 20 dB, (a) 90 symbols per subcarrier, (b) 900 symbols per subcarrier, (c) 90 symbols per subcarrier, and (d) 900 symbols per subcarrier. In this example, the QPSK center frequency is shifted 25 percent away from the LFM 3 dB frequency ($f_\Delta = 0.25$) for Figure 4.1 (a) and (b). This is a case where the spectral overlap between communications subcarriers may become significant (i.e., affect on symbol error rate). Moreover, Figure 4.1 (c) and (d) were generated with the QPSK center frequency shifted 50 percent away from the LFM 3 dB frequency ($f_\Delta = 0.5$). Moving the subcarrier frequencies away from the mainlobe increases the total bandwidth of the combined signal generated. Note that the SAR picture is closely similar to the baseline image, without discernable degradation to picture quality nor improvement in resolution. This is mostly due to very high RCR = 20 dB, where the LFM is too dominant compared to QPSK signal. There is very little to no discernable differences between SAR images of Figures 4.1. In other words, SAR images with similar resolution to the baseline are achieved with 90 and 900 symbols per subcarrier, whether $f_\Delta = 0.25$ or $f_\Delta = 0.5$. In future work, it is proposed to investigate in depth the effect on resolution of various parameters, especially if RCR is allowed to be only moderately high, or even lower.

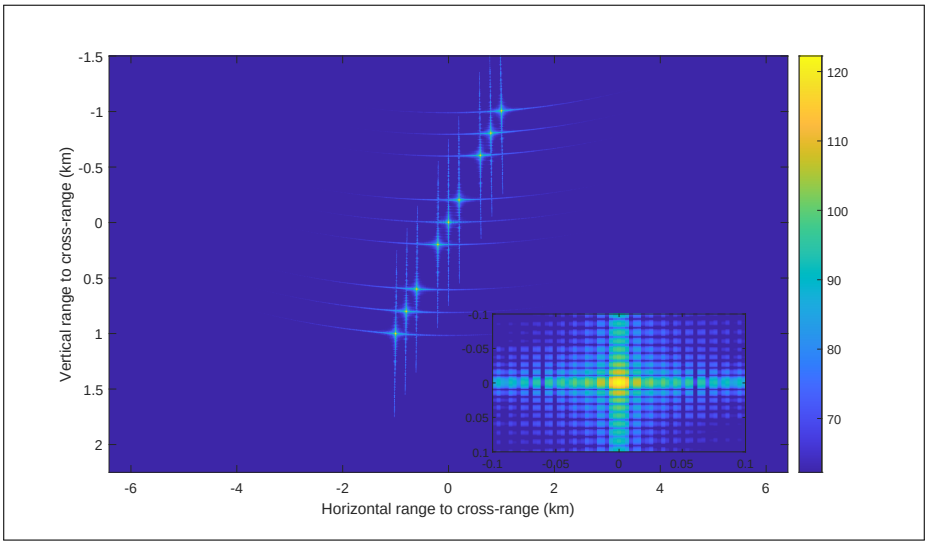

(a) 90 symbols and $f_\Delta = 0.25$

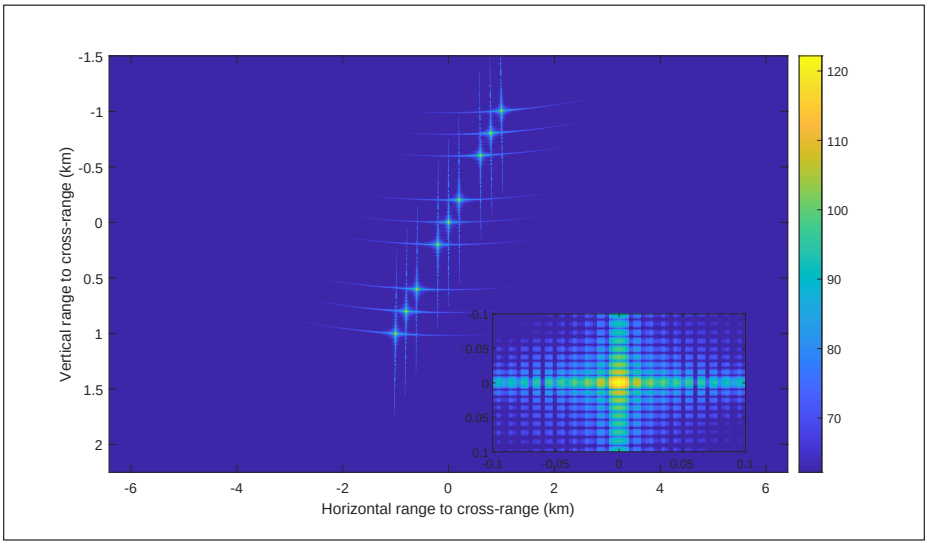

(b) 900 symbols and $f_\Delta = 0.25$

Figure 4.1. Generated SAR pictures and corresponding color bar [dB], with SNR=30 dB, and RCR=20 dB (continued on next page)

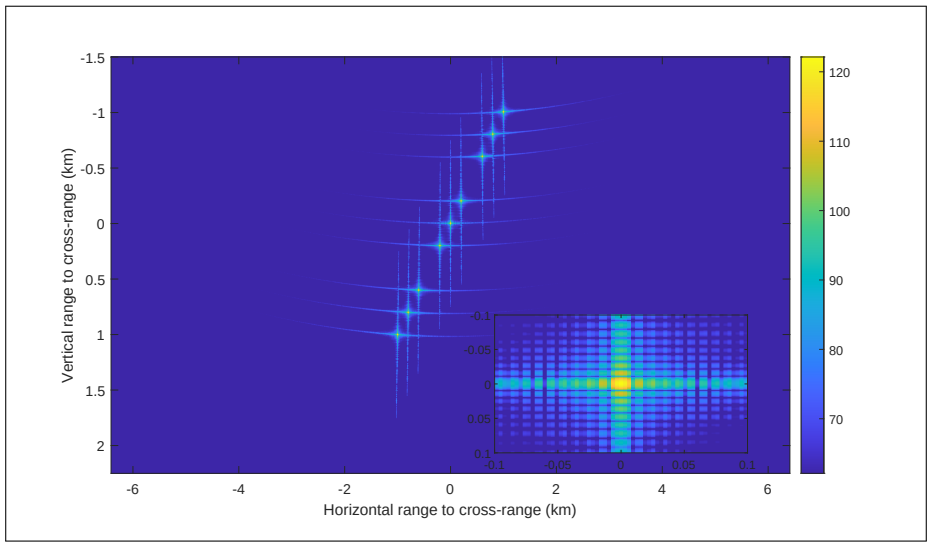

(c) 90 symbols and $f_\Delta = 0.50$

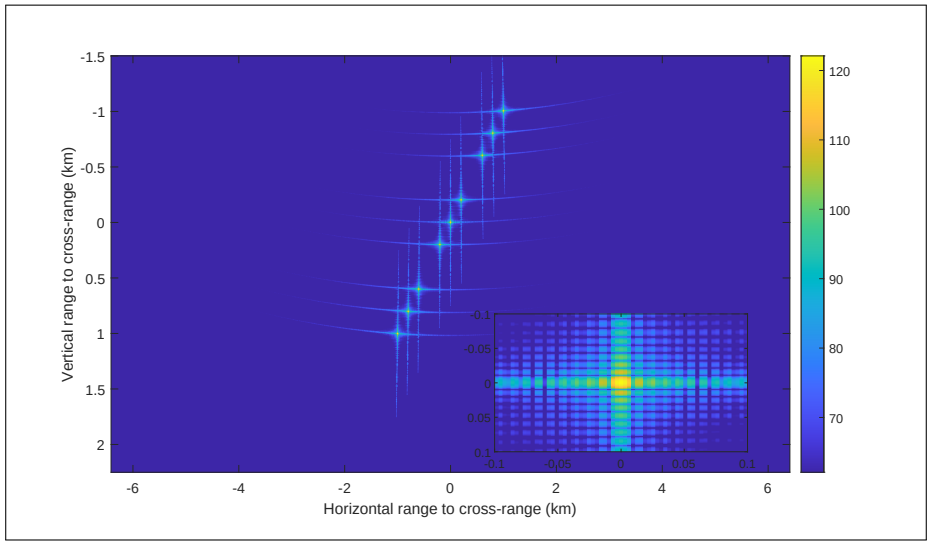

(d) 900 symbols and $f_\Delta = 0.50$

Figure 4.1. (continued from previous page) Generated SAR pictures and corresponding color bar [dB], with SNR=30 dB and RCR=20 dB

THIS PAGE INTENTIONALLY LEFT BLANK

CHAPTER 5:
Antenna Characterization with UAV Field Tests

Antennas are an important part of a SAR imaging system. A SAR system typically uses a directional antenna. Our chosen antenna is the Yagi antenna which turns out to be too large for the UAV. Thus, for the purpose of antenna-pair characterization, the Yagi is placed on the ground as the receiving antenna. A smaller whip antenna is placed on the drone. Antenna characterization is performed by generating received power radiation patterns in a 360° area for a given antenna setup. Again, the Yagi antenna is physically too big and heavy to fit on a drone-mounted system; an omni whip antenna is utilized to transmit from the drone. The characteristics of both antennas and the rest of the equipment are covered in following sections of Chapter 5.

5.1 Field Test Information

Field testing was conducted at McMillan Airfield, Camp Roberts, CA. The latitude and longitude (35.7987° N, 120.7434° W) can be observed in Figure 5.1. A signal generator and air whip antenna are attached to a drone. The generator is set to transmit a 10 dBmW continuous wave (CW) signal at 430, 450 and 470 MHz frequencies. A seven-element Yagi antenna capable of operating at 406-512 MHz. Inclination angles of 0° and 24° (with respect to ground) are utilized with the receiver on the ground. This set-up emulates a UAV antenna-pair, transmit-receive system that is important to characterize. The equipment details are discussed in the following sections. Various pictures of the actual field test are included in Appendix A.5.

Figure 5.1. Camp Roberts testing site

5.2 The Drone

The drone utilized is the Freefly Alta 8 model featured in Figure 5.2. This UAV is equipped with eight propellers, each with its own direct drive three-phase permanent magnet alternating current outrunner motor. The drone is chosen because it is manufactured in the United States and it is capable of carrying up to 20 lbs of load (while maintaining an average flight time of 20 min per set of batteries). It also has the "hold position" flight mode which allows the drone to maintain its position in the air through GPS positioning during the experiment.

Figure 5.2. Freefly Alta 8 drone. Source: [16].

Appendix Figure A.1 contains the Freefly Alta 8 datasheet provided by the manufacturer. More information can be found at https://freeflysystems.com/alta-8/specs.

5.3 The Signal Generator

The 10 dBmW CW test signals are generated utilizing a Vaunix signal generator, specifically, the LMS-152 D featured in Figure 5.3. This model generates signals ranging from 0.25 GHz up to 1.5 GHz. It is USB controlled and is fully programmable to produce the desired signals with an output power of -45 to +10 dBmW with low phase noise. The signal generator is lightweight (less than one pound), so it can be attached to the Alta 8, and is powered by a portable external battery. It transmits the desired signals while the drone is in flight. The LMS-152 D data sheet provided by the manufacturer is attached in Appendix section A.2. For more information on Vaunix technologies, visit https://vaunix.com/lms-152d-digital-signal-generator/.

Figure 5.3. Vaunix LMS-152 D signal generator. Source: [17].

5.4 The Transmitter Antenna

Figure 5.4 shows the transmitter antenna selected: PE51148, 1/4" wave omni whip antenna. This antenna is designed by Pasternack technologies [18] to operate in the 450-470 MHz frequency band, with a typical 0 dBi gain and an impedance of 50 Ω. The PE51148 data sheet is attached in Appendix A.3. For more information on Pasternack technologies, visit https://www.pasternack.com/

Figure 5.4. PE51148 transmitter antenna. Source: [18].

5.5 The Receiver Antenna

Figure 5.5 shows the receiver antenna selected: the 480-70 model produced by [19]. This seven-element, UHF Yagi directional antenna is designed to operate at frequencies in the range of 380-512 MHz. It has a gain of 10dBi and an impedance of 50 Ω.

The field test results are compared to the simulation patterns produced by FEKO, a commercial electromagnetic simulations software by Altair [20]. In Figure 5.6, the horizontal radiation pattern produced by FEKO is displayed on the left. The radiation pattern provided by the manufacturer is displayed on the right. Similarly, Figure 5.7 shows the vertical radiation pattern produced by FEKO on the left, while the radiation pattern provided by the manufacturer is displayed on the right. Note that these are for horizontal polarization. The data sheet provided by the manufacturer for the Yagi antenna and other models is attached in Appendix A.4.

Figure 5.5. UHF Yagi receiver antenna. Source: [19].

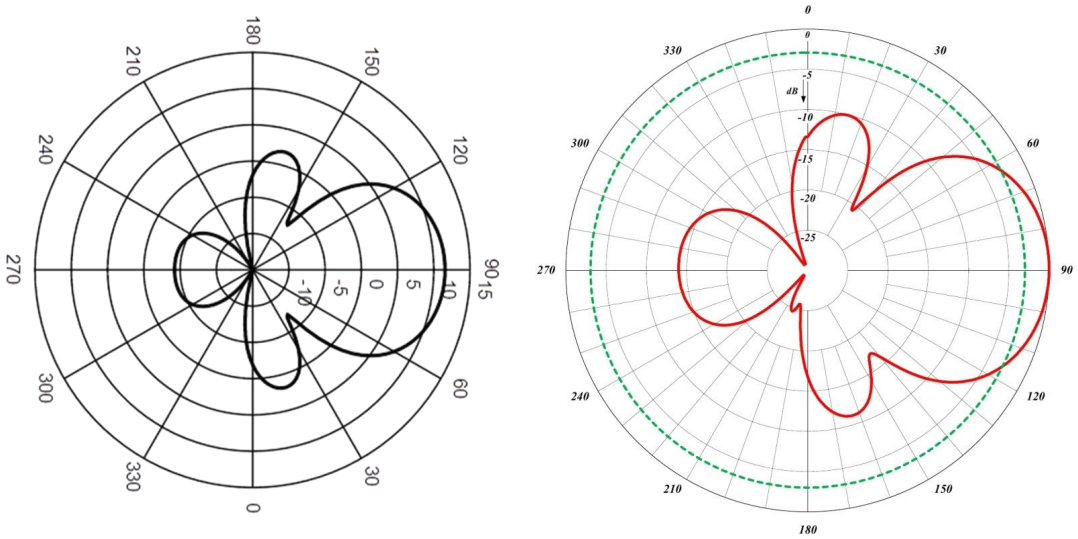

Figure 5.6. Receiver antenna vertical radiation pattern (horizontal polarization) produced by FEKO (left) vs the provided by manufacturer (right). Source: [19].

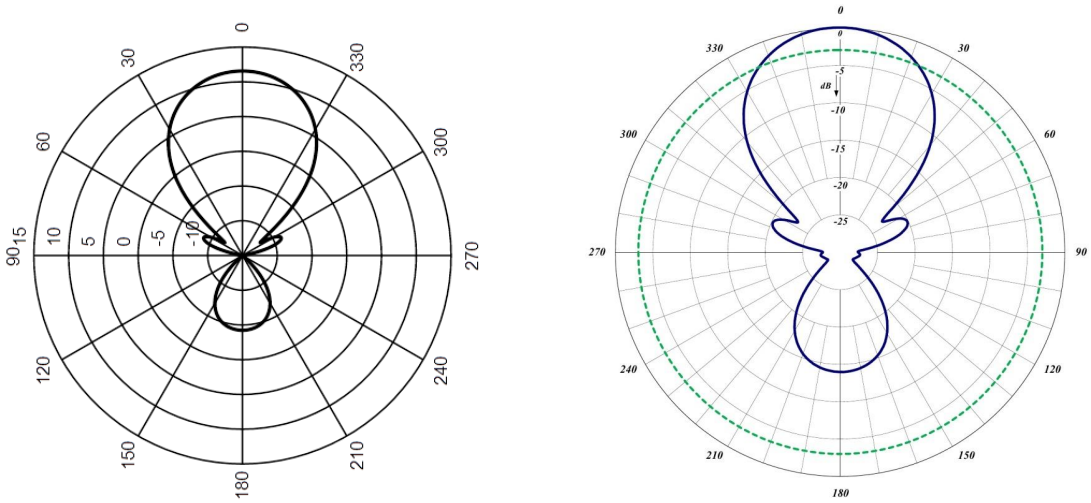

Figure 5.7. Receiver antenna vertical radiation pattern (horizontal polarization) produced by FEKO (left) vs the provided by manufacturer (right). Source: [19].

5.6 Cable and Antenna Loss

In RF systems, sources of loss must be accounted for. RF losses can be caused by equipment such as antennas, cable loss, and loose connectors among others. To account for these losses, the scattering parameters S_{11} reflection and S_{21} transmission tests are performed on the receiver front end. The S_{11} measures return loss on the receiver antenna. The antenna is connected to a vector network analyzer. The test then measures how much power is reflected and returned to the port. The S_{21} is a test that measures signal transmission loss due to the material, length, dielectrics and conductor resistance of the cable (used to connect the antenna to the receiver). For these measurements, the impedance is 50 Ω. The results of the receiver antenna S_{11} and cable S_{21} tests are displayed in Figures 5.8 and 5.9, respectively. The results show that the antenna has a negligible reflection loss (0 dB) and the cable has around 0.5 dB of insertion loss.

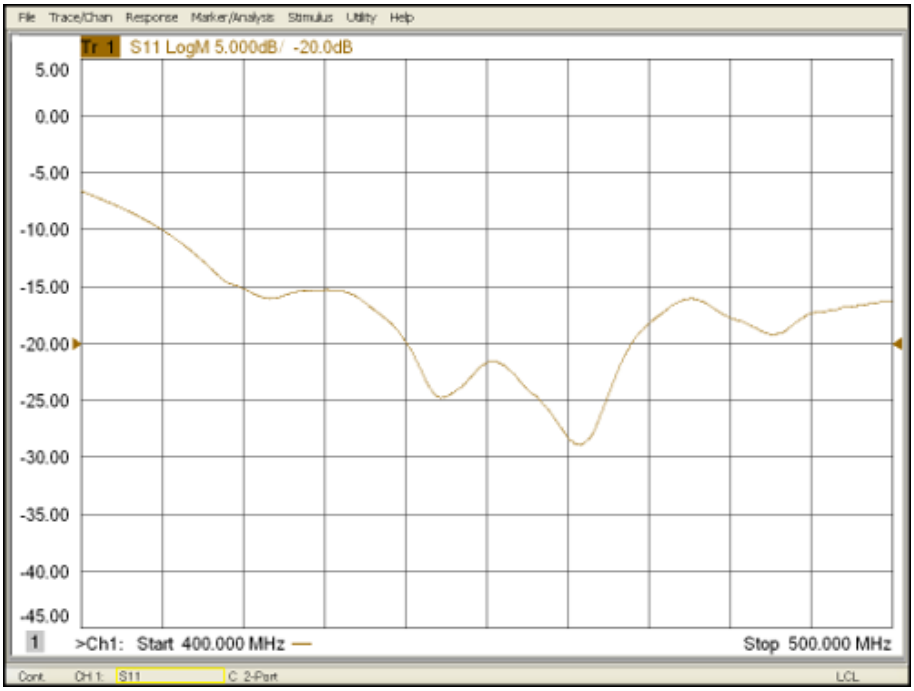

Figure 5.8. Receiver antenna S_{11} test result

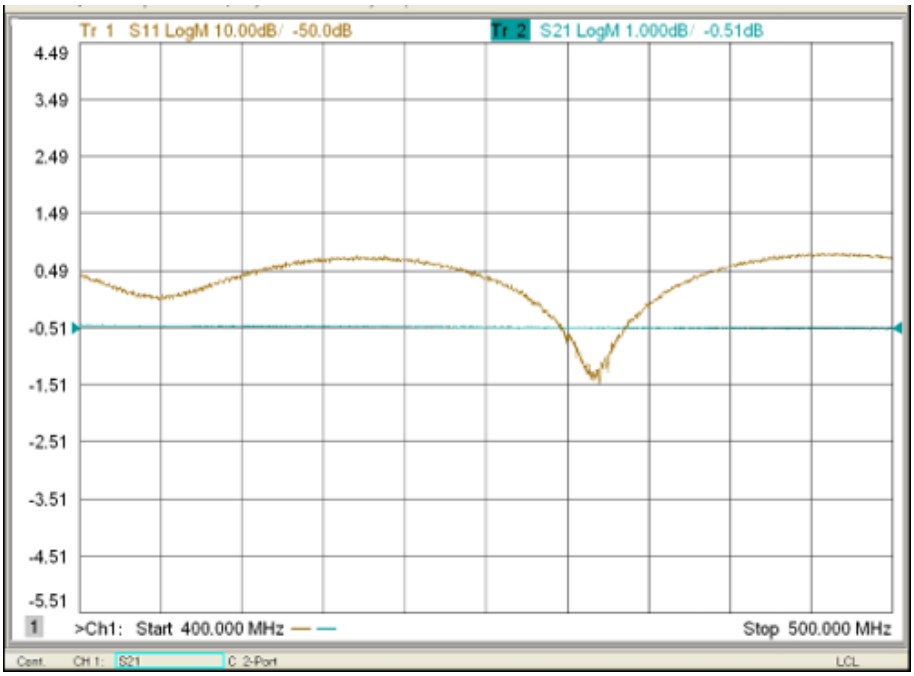

Figure 5.9. Cable S_{21} test result

THIS PAGE INTENTIONALLY LEFT BLANK

CHAPTER 6:
Field Experiments and Results

6.1 Experiments 1-3: Receiver Antenna at 0° Inclination

Six experiments are conducted utilizing the equipment discussed in Chapter 5. This section discusses the setup for the first three as shown in Figure 6.1. The receiver antenna is placed on the ground receiver platform with an inclination angle $\phi = 0^\circ$ with respect to the ground. Note the Yagi antenna is positioned such that vertical polarization is utilized. In other words, the mainbeam is pointed at 0° from the ground level. The signal generator is attached to the Alta 8 and is set to transmit a 10 dBmW continuous wave (CW) signal at 430, 450, or 470 MHz frequency. The drone is placed at an altitude h with respect to ground. Although wind is present, the altitude does not vary greatly due to the drone "hold position" via GPS control. However, each experiment has slightly different height, since we're not able to replicate the exact geometry of each experiment. For example, $h = 95.5$ ft for Experiment 1. L is the horizontal distance between transmitter and receiver antennas. For Experiment 1, $L = 98.4$ ft. Slant range is defined as the straight-line distance between transmitter and receiver antennas (calculated to be 137 ft for Experiment 1). The angle θ is defined as the angle between the receiver antenna and the drone. The drone is placed in position and held in place while testing is in progress. The receiver antenna is aligned at the 0° position. A 10 dBmW CW signal is transmitted by the LMS-152 D. The signal is received by the Yagi antenna, and the received power is recorded. Then, the Yagi antenna is rotated 10° in azimuth, and the corresponding received power is recorded. The process is repeated until the receiver antenna has been rotated 180°.

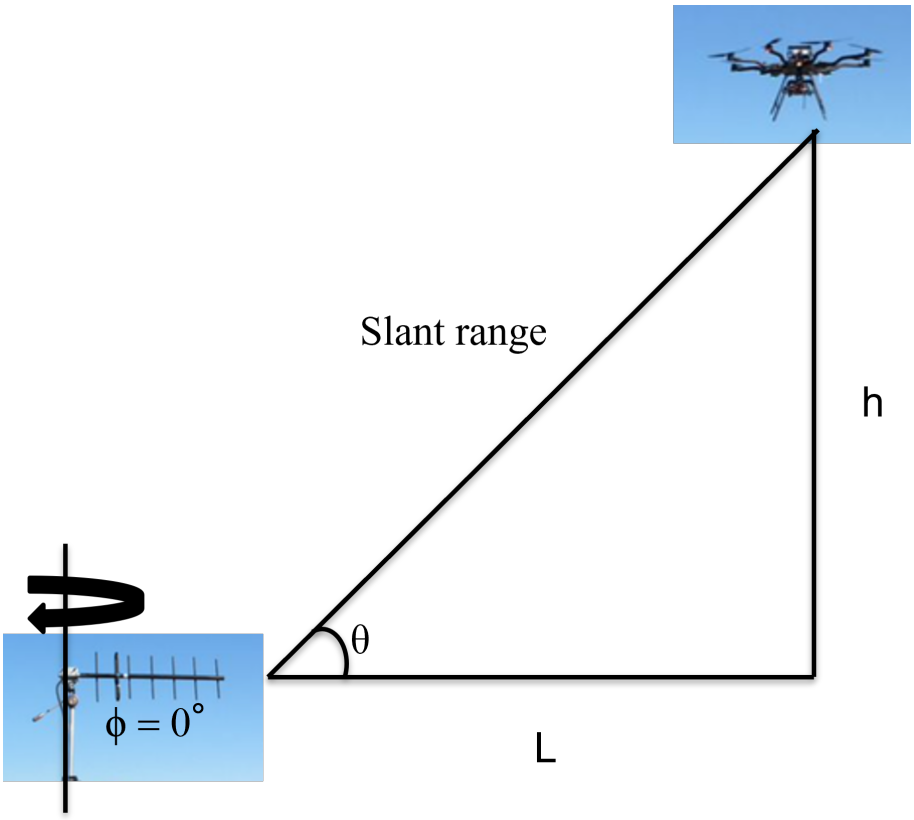

Figure 6.1. Experiments 1-3 setup

6.2 Experiments 4-6: Receiver Antenna at 24° Inclination

The field test set up for Experiments 4-6 is the same as in Experiments 1-3, except that the receiver antenna has an inclination angle $\phi = 24°$ with respect to the ground (where vertical polarization is utilized). In other words, the mainbeam is partially pointed toward the transmitter as shown in Figure 6.2. The drone is placed in position and held in place while testing is in progress. A 10 dBmW CW signal is transmitted by the LMS-152 D. The signal is received by the Yagi antenna, and the received power is recorded. Then, the Yagi antenna is rotated 10° in azimuth, and the corresponding received power is recorded. The process is repeated until the receiver antenna has been rotated 180°.

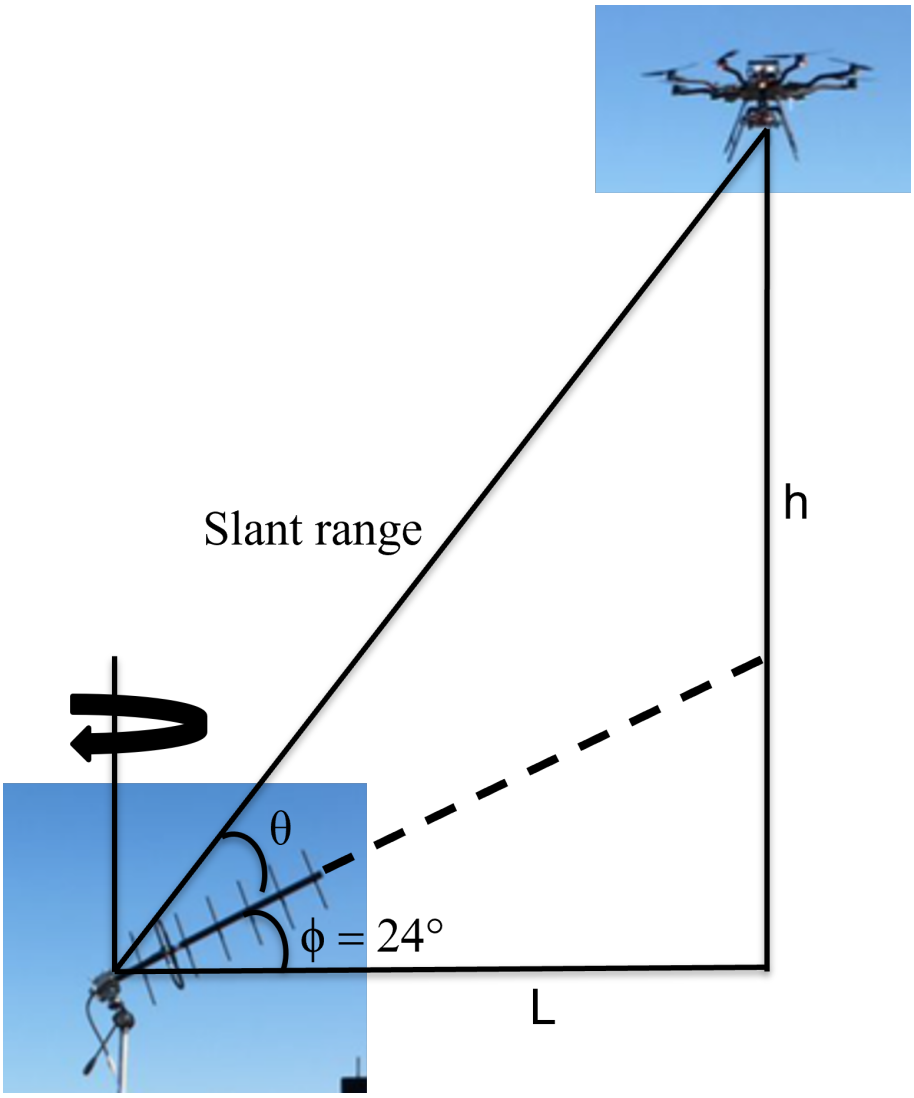

Figure 6.2. Experiments 4-6 setup

6.3 Results

This section analyzes and compares the measured power received versus expected received power for each experiment. In this section, while we report the measured power at various azimuth angles, we also compare expected maximum power received to the measured power (at the direction of the main beam), based on the distance between the transmitter and receiver. For free space line of sight propagation, the power received (P_r), is given by:

$$P_r = P_t G_t G_r (\lambda/(4\pi d))^2, \tag{6.1}$$

where P_t is the power transmitted (10 dBmW for this work), G_t is the gain of the transmitter antenna (0 dBi for this work), G_r is the gain of the receiver antenna (which varies depending on receiver antenna inclination), reduced by cable loss. The wavelength is $\lambda = c/f$, and $c = 3x10^8$ m/s (speed of light). We assume a 2 dB less gain for 430 MHz and 470MHz (compared to the 450 MHz center frequency).

The measured power at the Yagi receiver antenna should be close to the value calculated utilizing Equation 6.1. Equation 6.1 does not consider reflections from the ground or other obstacles in the environment. The experiments only measured power received by the Yagi antenna from $0 - 180°$. Therefore, it is important to note that Figures 6.3-6.8 are generated by replicating or "mirroring" the $0 - 180°$ measured power to the other half of the plane in order to complete a 360° pattern.

6.3.1 Experiment 1

The power received during Experiment 1 by the receiver on the ground is displayed in Figure 6.3. The parameters for the experiment along with the expected and measured received power (main beam: 0° only) are shown in Table 6.1. The transmit frequency was f = 430 MHz. The receiver antenna inclination was ϕ = 0°. The vertical distance to the drone was h = 95.5 ft. The horizontal distance to the drone was L = 98.4 ft. The slant range between transmitter and receiver was 137.1 ft. The angle between the drone and ground, with the receiver antenna used as vertex, was θ = 44.1°

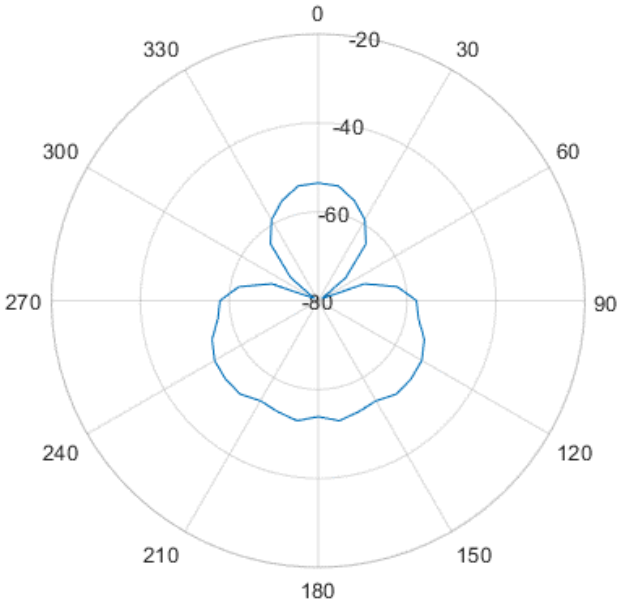

Figure 6.3. Measured power pattern vs. rotation angle θ, from the receiver on the ground during Experiment 1 [dBmW]: f = 430 MHz and ϕ = 0°

Table 6.1. Experiment 1 parameters and results

Variable	Value	Units
f	430	MHz
ϕ	0	deg
h	95.5	ft
L	98.4	ft
Slant range	137.1	ft
θ	44.1	deg
Expected received power	-46.0	dBmW
Measured received power	-52.6	dBmW

6.3.2 Experiment 2

The power received during Experiment 2 by the receiver on the ground is displayed in Figure 6.4. The parameters for the experiment along with the expected and measured received power (main beam: 0° only) are shown in Table 6.2. The transmit frequency was f = 450 MHz. The receiver antenna inclination was ϕ = 0°. The vertical distance to the drone was h = 96 ft. The horizontal distance to the drone was L = 98 ft. The slant range between transmitter and receiver was 137.2 ft. The angle between the drone and ground, with the receiver antenna used as vertex, was θ = 44.4°

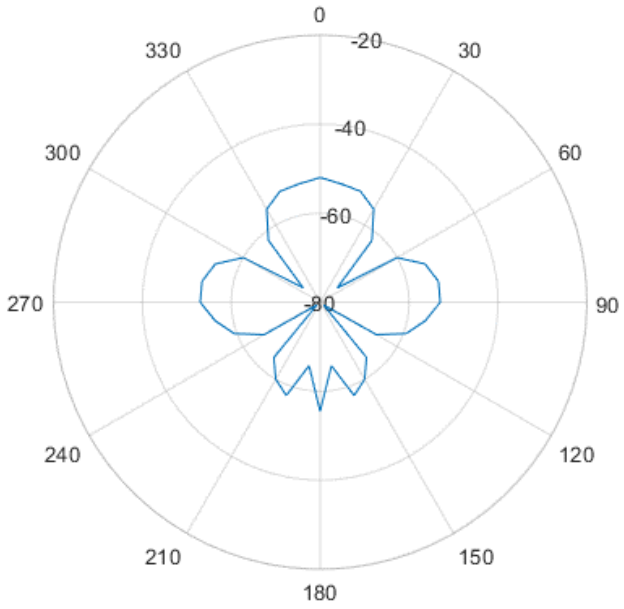

Figure 6.4. Measured power pattern vs. rotation angle θ, from the receiver on the ground during Experiment 2 [dBmW]: $f = 450$ MHz and $\phi = 0°$

Table 6.2. Experiment 2 parameters and results

Variable	Value	Units
f	450	MHz
ϕ	0	deg
h	96.0	ft
L	98.0	ft
Slant range	137.2	ft
θ	44.4	deg
Expected received power	-44.4	dBmW
Measured received power	-52.0	dBmW

6.3.3 Experiment 3

The power received during Experiment 3 by the receiver on the ground is displayed in Figure 6.5. The parameters for the experiment along with the expected and measured received power (main beam: 0° only) are shown in Table 6.3. The transmit frequency was f = 470 MHz. The receiver antenna inclination was ϕ = 0°. The vertical distance to the drone was h = 95 ft. The horizontal distance to the drone was L = 97.5 ft. The slant range between transmitter and receiver was 136.1 ft. The angle between the drone and ground, with the receiver antenna used as vertex, was θ = 44.3°

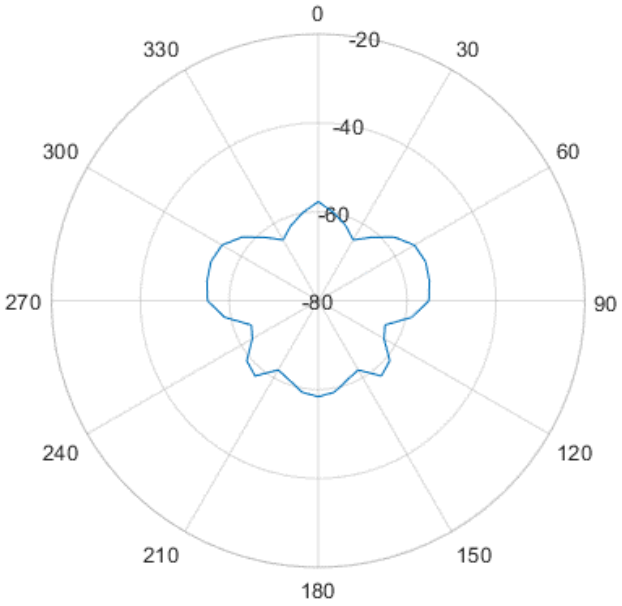

Figure 6.5. Measured power pattern vs. rotation angle θ, from the receiver on the ground during Experiment 3 [dBmW]: f = 470 MHz and ϕ = 0°

Table 6.3. Experiment 3 parameters and results

Variable	Value	Units
f	470	MHz
ϕ	0	deg
h	95.0	ft
L	97.5	ft
Slant range	136.1	ft
θ	44.3	deg
Expected received power	-46.8	dBmW
Measured received power	-54.3	dBmW

6.3.4 Experiment 4

The power received during Experiment 4 by the receiver on the ground is displayed in Figure 6.6. The parameters for the experiment along with the expected and measured received power (main beam: 24° only) are shown in Table 6.4. The transmit frequency was f = 430 MHz. The receiver antenna inclination was ϕ = 24°. The vertical distance to the drone was h = 95 ft. The horizontal distance to the drone was L = 98 ft. The slant range between transmitter and receiver was 136.5 ft. The angle between the drone and ground, with the receiver antenna used as vertex, was θ = 44.1°.

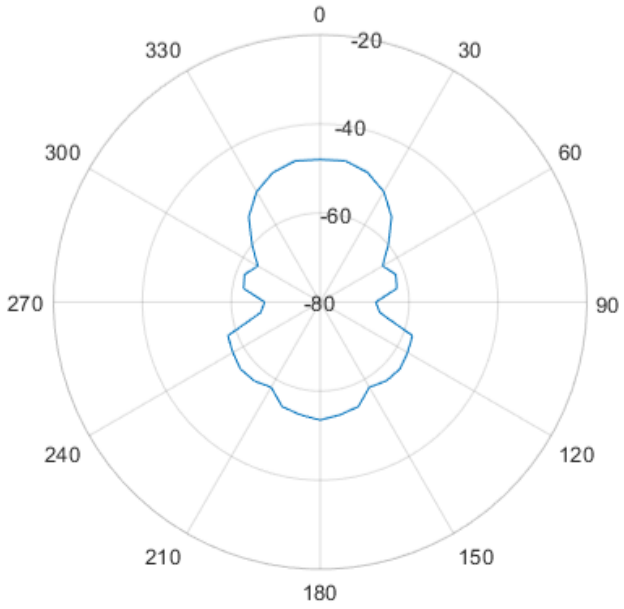

Figure 6.6. Measured power pattern vs. rotation angle θ, from the receiver on the ground during Experiment 4 [dBmW]: $f = 430$ MHz and $\phi = 24°$

Table 6.4. Experiment 4 parameters and results

Variable	Value	Units
f	430	MHz
ϕ	24	deg
h	95.0	ft
L	98.0	ft
Slant range	136.5	ft
θ	44.1	deg
Expected received power	-43.0	dBmW
Measured received power	-47.8	dBmW

6.3.5 Experiment 5

The power received during Experiment 5 by the receiver on the ground is displayed in Figure 6.7. The parameters for the experiment along with the expected and measured received power (main beam: 24° only) are shown in Table 6.5. The transmit frequency was f = 450 MHz. The receiver antenna inclination was ϕ = 24°. The vertical distance to the drone was h = 94.7 ft. The horizontal distance to the drone was L = 98.8 ft. The slant range between transmitter and receiver was 136.9 ft. The angle between the drone and ground, with the receiver antenna used as vertex, was θ = 43.8°

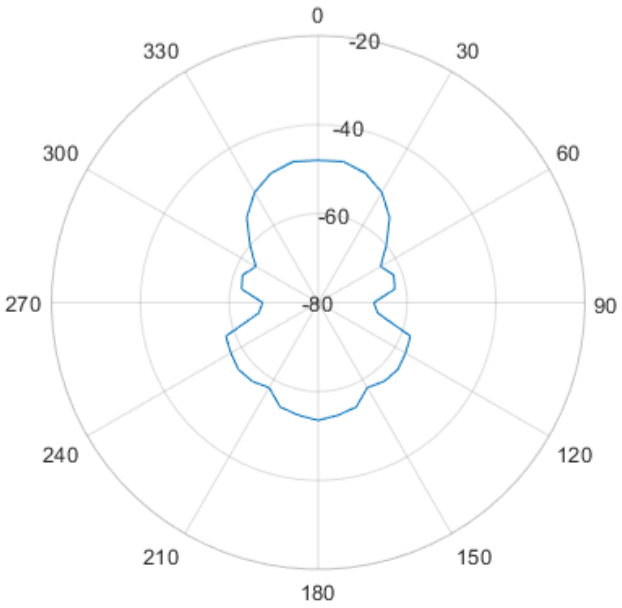

Figure 6.7. Measured power pattern vs. rotation angle θ, from the receiver on the ground during Experiment 5 [dBmW]: f = 450 MHz and ϕ = 24°

Table 6.5. Experiment 5 parameters and results

Variable	Value	Units
f	450	MHz
ϕ	24	deg
h	94.7	ft
L	98.8	ft
Slant range	136.9	ft
θ	43.8	deg
Expected received power	-41.4	dBmW
Measured received power	-44.9	dBmW

6.3.6 Experiment 6

The power received during Experiment 6 by the receiver on the ground is displayed in Figure 6.8. The parameters for the experiment along with the expected and measured received power (main beam: 24° only) are shown in Table 6.6. The transmit frequency was f = 470 MHz. The receiver antenna inclination was ϕ = 24°. The vertical distance to the drone was h = 95 ft. The horizontal distance to the drone was L = 97.5 ft. The slant range between transmitter and receiver was 136.1 ft. The angle between the drone and ground, with the receiver antenna used as vertex, was θ = 44.3°

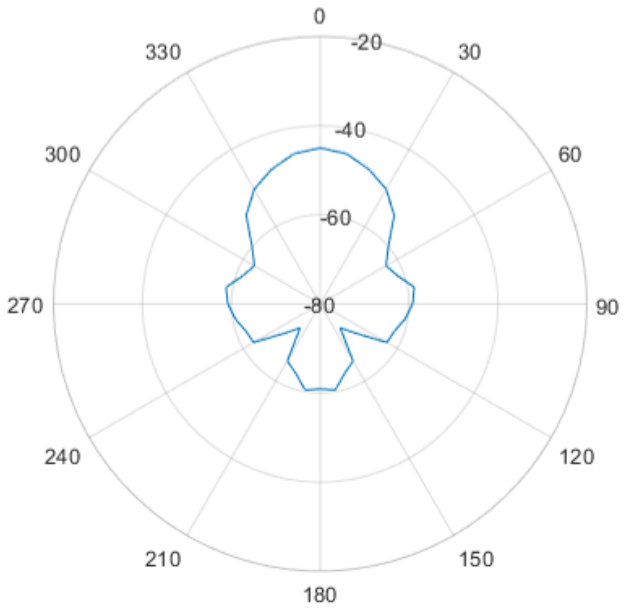

Figure 6.8. Measured power pattern vs. rotation angle θ, from the receiver on the ground during Experiment 6 dBmW]: $f = 470$ MHz and $\phi = 24°$

Table 6.6. Experiment 6 parameters and results

Variable	Value	Units
f	470	MHz
ϕ	24	deg
h	95.0	ft
L	97.5	ft
Slant range	136.1	ft
θ	44.3	deg
Expected received power	-43.8	dBmW
Measured received power	-45.0	dBmW

6.3.7 Results Discussion

Table 6.7 summarizes the results from Experiments 1-6 in one table for quick comparison of the expected received power and measured received power from Tables 6.1-6.6. Adding an inclination of $\phi = 24°$ on the receiver antenna increased the measured received power due to the antenna pointing towards the UAV. The largest received power was obtained from Experiment 5, with an inclination of $\phi = 24°$ at a frequency $f = 450$ MHz (as may be expected). The received power measured for all experiments was lower than the theoretically expected received power, but within the range of expected values. The differences may be attributed to a variety of factors such as scattering, crystal drift (noticeable), angle precision, and human measurement error, among others. It is important to note that the relatively short life of the batteries (around 20 minutes depending on load) caused the necessity to land and relaunch the drone for every experiment, thereby slightly varying geometry parameters of the experiment.

Table 6.7. Measured power (at receiver) per experiment [dBmW]

	Experiment 1	Experiment 2	Experiment 3
expected max	-46.0	-44.4	-46.8
measured max	-52.6	-52.0	-54.3
	Experiment 4	Experiment 5	Experiment 6
expected max	-43.0	-41.4	-43.8
measured max	-47.8	-44.9	-45.0

THIS PAGE INTENTIONALLY LEFT BLANK

CHAPTER 7:
Summary and Conclusions

Chapter 1 of this thesis provided background information and explained the objectives. Then, in Chapters 2 through 4, we separately added two QPSK subcarriers into the guardbands of a LFM waveform used for SAR imaging. The goal was to produce a SAR picture of similar or better resolution (if possible) than an image produced by the LFM waveform by itself. In theory, adding the QPSK signal increased the total bandwidth of the transmit signal. The idea was to use the combined signal in the receiver without having to filter out the QPSK signals. Parameters such as LCBR (or SRBR) and subcarrier shift were varied in an attempt to investigate the effects of various parameters to the SAR images. So long as the RCR and SNR were large, and the subcarriers were in the guardband proper, there was no discernable effect to the quality of the SAR images. We used 9, 90, and 900 symbols with an RCR = 20 dB, SNR = 30 dB, $f_\Delta = 0.25$ and $f_\Delta = 0.5$. Moreover, there seemed to be little discernable improvement in range resolution since the communications signal is low-power.

In Chapters 5 and 6, we discussed the field testing for antenna characterization. Received power via transmitted signal from the Alta 8 drone, with a "brick" signal generator as the transmitter. The power received on the ground was recorded using a "brick" spectrum analyzer. Two inclination angles were used for the Yagi receive antenna. Drone flight time was a function of payload and battery life. The measured received power varied between one and eight dBmW from the free-space, one-path propagation expected received power. The difference is attributed to the presence of multipath and antenna pointing accuracy.

7.1 Future Work

This thesis did not look in depth at how resolution is improved by using the QPSK signals placed in the guardbands when radar power and communications power were comparable. In future work, we propose to quantify the difference in resolution between the SAR images produced by the baseline LFM signal and the combined LFM-QPSK signal. It is proposed to use a lower RCR in future work to see discernable difference in image quality. That study may cause significant change to the SAR images, although, this might not be practical nor

desired by the radar system. Other interesting aspects and parameters that affect SAR images that can also be investigated are: effects of signal sidelobe levels, various noise and clutter effects, contrast metrics, communications symbol pulse shaping, and information-theoretic metrics.

Research into extending the flight time of the drone with a higher payload is also of interest. If payload and flight time were not an issue, it would be feasible to develop a drone capable of generating a SAR picture while simultaneously transmitting it as a communications signal to a receiver on the ground.

APPENDIX:

A.1 Freefly Alta 8 Data Sheet

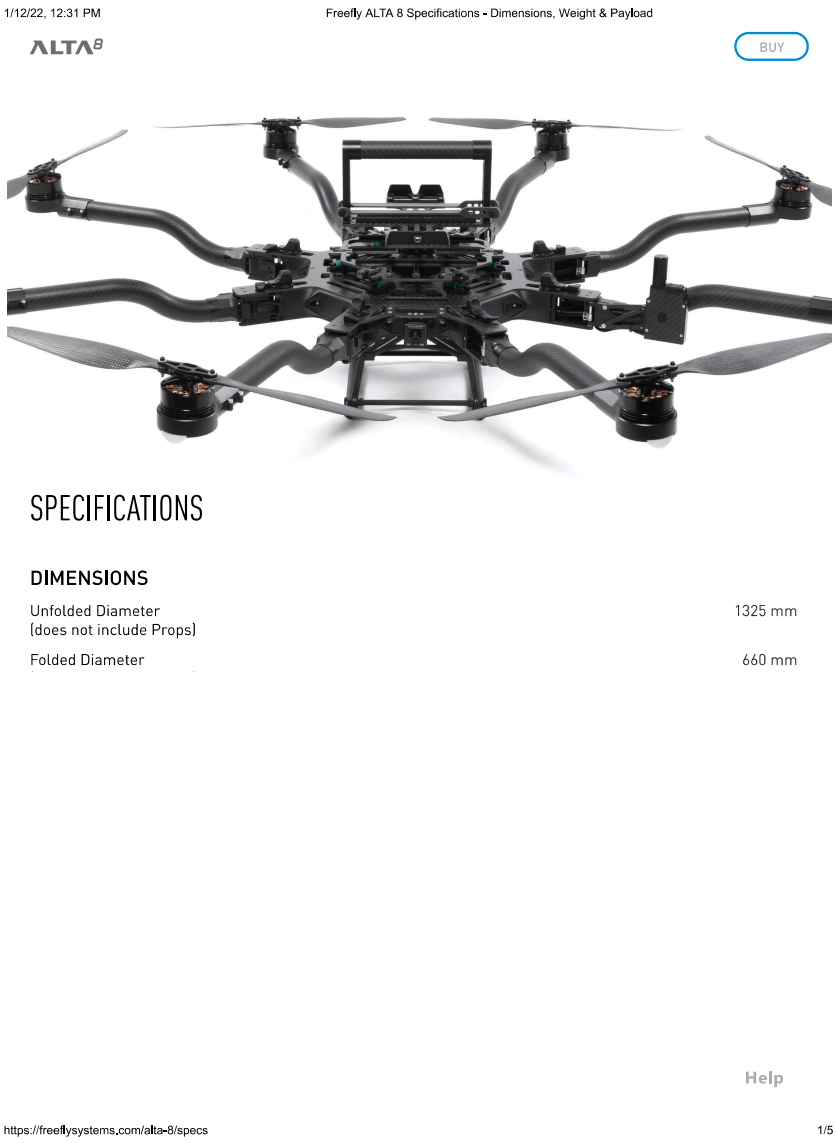

1/12/22, 12:31 PM Freefly ALTA 8 Specifications - Dimensions, Weight & Payload

ALTA 8

BUY

SPECIFICATIONS

DIMENSIONS

Unfolded Diameter (does not include Props)	1325 mm
Folded Diameter	660 mm

Help

https://freeflysystems.com/alta-8/specs 1/5

Figure A.1. Freefly Alta 8 data sheet. Source: [16](page 1).

ALTA 8 BUY

Propeller Orientation	(4) CW and (4) CCW Props
Propeller Type	18 x 6 Folding

BATTERY

Nominal Battery Voltage	6S / 22.2V
Maximum Battery Size	240 x 180 x 80 mm
Maximum Battery Quantity	2 Battery Packs (Parallel)
Minimum Battery Quantity	2 Battery Packs (Parallel)
Battery Connectors	2x EC5 (Parallel)
Required Minimum Battery Discharge Rating	250A / 500A Peak

WEIGHTS

Maximum Gross for Takeoff[1]	18.1 kg (40.0 lbs)
Maximum Useful Load[2]	12.0 kg (26.4 lbs)
Maximum Payload[3]	9.1 kg (20.0 lbs)
Typical Standard Empty Weight	6.2 kg (13.6 lbs)

WARNING

Always refer to the following aircraft limitations section for complete information on allowable maximum gross weights at different altitudes and temperatures before any flight.

Help

Figure A.1. Freefly Alta 8 data sheet. Source: [16] (page 2).

ALTA 8 BUY

Supported Radio Controller Telemetry Systems	Futaba w/ built-in voltage sense port
Minimum Radio Controller Channels Required	>5
Supported GNSS	GPS, GLONASS, Galileo
Supported SBAS	QZSS, WAAS, EGNOS, MSAS
First-Person View System Video Formats	NTSC, PAL
Supported First-Person View Transmitters	Skyzone BOSCAM Immersion RC Fatshark
Supported First-Person View Cameras	Ready Made RC
First-Person View OSD Telemetry	User Configurable
Installed Transceivers	Wi-Fi
Data Logging Rate	25 Hz

LIGHTING AND INDICATION

Status Light	1-Watt Red, 1-Watt White LED
Orientation Lights	3-Watt RGB LED
Orientation Light Color	Red, Yellow, Blue, Green, White

ISOLATION SYSTEM

Vibration Isolation System	Silicone O-Rings

ISOLATION SYSTEM OPTIONS:

Help

Figure A.1. Freefly Alta 8 data sheet. Source: [16] (page 3).

ALTA 8

BUY

Maximum Battery Voltage	25.2 Volts
Minimum Average Battery Voltage	19.2 Volts

ENVIRONMENTAL LIMITATIONS

Do not fly ALTA 8 in temperatures exceeding 45°C (113°F) or below -20°C(-4°F).[5]

FLIGHT CONTROLLER LIMITS

Maximum Pitch/Roll Angle	45°
Maximum Yaw Rate	150° / second

1. At sea level, standard conditions.
2. Top and bottom mount. Includes batteries.
3. Payload weight top or bottom mount. Battery weight not included and mounted on opposite side from payload in typical configurations.
4. At maximum takeoff weight, sea level, standard conditions.
5. Must additionally observe battery temperature ratings.

COMMUNITY

Help

Figure A.1. Freefly Alta 8 data sheet. Source: [16] (page 4).

A.2 Vaunix Signal Generators Data Sheet

Figure A.2. Vaunix signal generator data sheet. Source: [17](page 1).

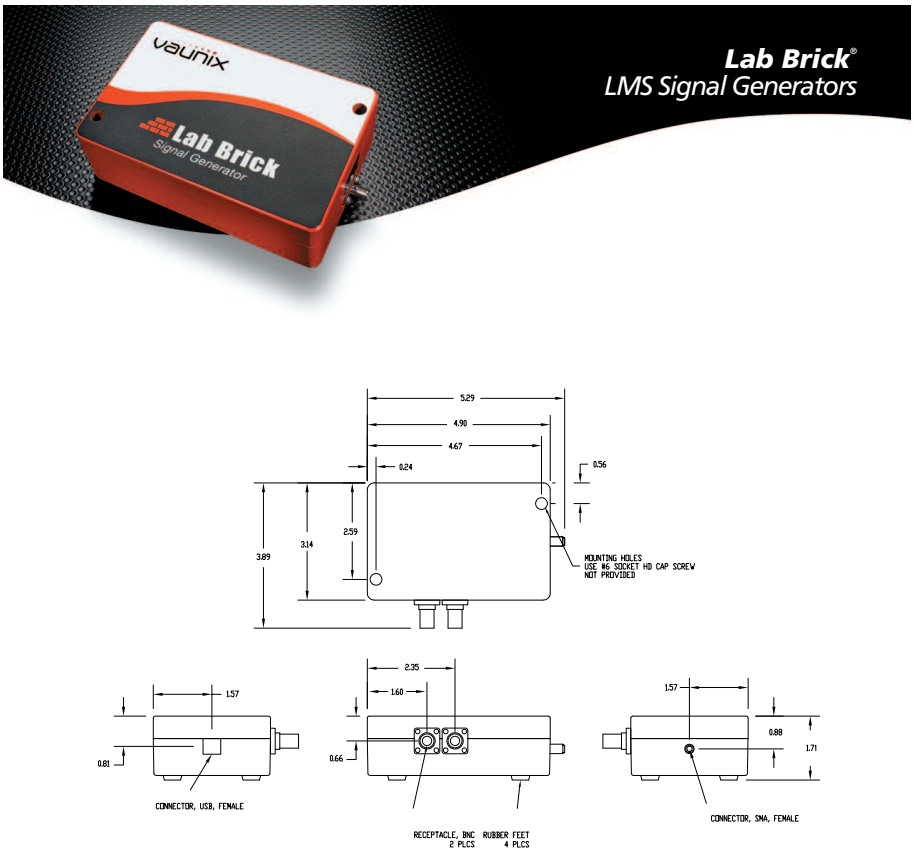

See performance graphs online at www.vaunix.com

vaunix
Vaunix Technology Corporation
7 New Pasture Road, Newburyport, MA 01950
978-662-7839 | www.Vaunix.com

RoHS COMPLIANT

Figure A.2. Vaunix signal generator data sheet. Source: [17] (page 2).

A.3 Transmitter Antenna Data Sheet

PASTERNACK
THE ENGINEER'S RF SOURCE

Whip Antenna Operates From 450 MHz to 470 MHz With a Typical 0 dBi Gain SMA Female Input Connector IP67 Rated

TECHNICAL DATA SHEET **PE51148**

Pasternack's ¼ wave portable omni whip antennas feature a textured black finish and a strain-relief base to ensure durability and repeatable RF performance. Our ¼ wave portable omni whip antennas are availabile with operating frequencies as low as 400 MHz and as high as 960 MHz. These antennas are offered with gain ranges from unity to 2 dBi. The omni-directional radiation pattern and IP67 rating make these antennas ideal for mobile radio communications.

- Operating frequencies from 400 MHz to 960 MHz
- Gain ranges from unity to 2 dBi
- VSWR less than 2:1, in most cases
- 50 Ohm Impedance
- IP67 Rated
- Variety of connector types available (SMA Female, MX, or MD) for use in many portable handheld radio applications. See below for common brand & connector combinations.
- MX (1/4-32 x 7/32) – Commonly used in: Motorola, Radius, Saber, Saber+, Spirit, Expo, Kenwood, Maxon, Midland, Wilson, GE Monogram, and Vertex Standard.
- MD (M7 x 1.0) – Commonly used in: GE
- SMA Female (SF) – Commonly used in: Motorola, Visar, and Kenwood

Configuration

Design	Whip Portable
Frequency Range	450 to 470 MHz
Polarization	Vertical
Interface 1	SMA Female
Number of Output Ports	1

Electrical Specifications (Values at 25°C, sea level)

Description	Minimum	Typical	Maximum	Units
Impedance		50		Ohms
Typical Gain	0			dBi
Input VSWR			2:1	

Mechanical Specifications

Radome Material	TPE
Size	
Length	6.06 in [153.92 mm]
Width	0.58 in [14.73 mm]
Weight	0.033 lbs [14.97 g]

Environmental Specifications

Temperature	
Operating Range	-20 to +65 deg C
Environment	IP67

Click the following link (or enter part number in "SEARCH" on website) to obtain additional part information including price, inventory and certifications: Whip Antenna Operates From 450 MHz to 470 MHz With a Typical 0 dBi Gain SMA Female Input Connector IP67 Rated PE51148

Pasternack Enterprises, Inc. • P.O. Box 16759, Irvine, CA 92623
Phone: (866) 727-8376 or (949) 261-1920 • **Fax:** (949) 261-7451
Sales@Pasternack.com • Techsupport@Pasternack.com

Figure A.3. PE51148 data sheet. Source: [18] (page 1).

PASTERNACK®
THE ENGINEER'S RF SOURCE

Whip Antenna Operates From 450 MHz to 470 MHz With a Typical 0 dBi Gain SMA Female Input Connector IP67 Rated

TECHNICAL DATA SHEET **PE51148**

Compliance Certifications (visit www.Pasternack.com for current document)
RoHS Compliant

Plotted and Other Data
Notes:
• Values at 25 °C, sea level

Outline Drawing

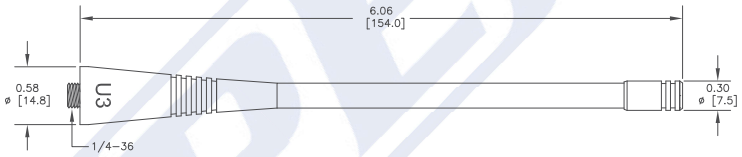

Click the following link (or enter part number in "SEARCH" on website) to obtain additional part information including price, inventory and certifications: Whip Antenna Operates From 450 MHz to 470 MHz With a Typical 0 dBi Gain SMA Female Input Connector IP67 Rated PE51148

Pasternack Enterprises, Inc. • P.O. Box 16759, Irvine, CA 92623
Phone: (866) 727-8376 or (949) 261-1920 • **Fax:** (949) 261-7451
Sales@Pasternack.com • Techsupport@Pasternack.com

Figure A.3. PE51148 data sheet. Source: [18] (page 2).

PASTERNACK®
THE ENGINEER'S RF SOURCE

Whip Antenna Operates From 450 MHz to 470 MHz With a Typical 0 dBi Gain SMA Female Input Connector IP67 Rated

TECHNICAL DATA SHEET **PE51148**

Whip Antenna Operates From 450 MHz to 470 MHz With a Typical 0 dBi Gain SMA Female Input Connector IP67 Rated from Pasternack Enterprises has same day shipment for domestic and International orders. Our RF, microwave and millimeter wave products maintain a 99% availability and are part of the broadest selection in the industry.

Click the following link (or enter part number in "SEARCH" on website) to obtain additional part information including price, inventory and certifications: Whip Antenna Operates From 450 MHz to 470 MHz With a Typical 0 dBi Gain SMA Female Input Connector IP67 Rated PE51148

URL: http://www.pasternack.com/single-antenna-450-470-mhz-0-dbi-gain-sma-pe51148-p.aspx

Pasternack Enterprises, Inc. • P.O. Box 16759, Irvine, CA 92623
Phone: (866) 727-8376 or (949) 261-1920 • **Fax:** (949) 261-7451
Sales@Pasternack.com • Techsupport@Pasternack.com

Figure A.3. PE51148 data sheet. Source: [18] (page 3).

A.4 Receiver Antenna Data Sheet

BASE STATION ANTENNAS

UHF YAGI ANTENNA HEAVY DUTY available BLACK ANODIZED available **380-512 MHz**

UHF Yagi Antennas Series

The UHF Yagi Antenna Series is available in 2, 3, 7 and 12 elements and our 70 MHz wideband configurations. By default, our Yagi antennas are end mounted. But a center mount or an extended boom are also available for certain models. All our antennas can be completely customized to your specific applications.

- Each antenna has a rugged, fully welded design to withstand harsh environmental conditions.
- Our antennas can be black anodized, and heavy-duty versions are available.
- The mounting hardware supplied allows either vertical or horizontal polarization.
- Please contact our Technical Support team for consultation.

Electrical Specifications	F-3872	433-70	430-70	480-70	437-70
Frequency Range, MHz (in splits)	406-470	406-470	380-512	406-470	450-512
Nominal Gain, dBd	3.5	6.5	10.0	10.0	12.0
Number of Elements	2	3	7	7	12
Bandwidth 1.5:1 VSWR, MHz (Center Freq. %)	24	24	24	64	62
Polarization	Vertical or Horizontal				
Horizontal Beamwidth (Vert. Pol.)	138º	83º	62º	62º	36º
Vertical Beamwidth (Vert. Pol.)	72º	59º	48º	50º	32º
Front to Back, dB	10	12	20	17	20
Pattern	Directional				
Power Rating, Watts	350	350	350	350	350
Nominal Impedance, Ohms	50	50	50	50	50
Lightning Protection	DC Ground				
Standard Termination	Type N Male				
Mechanical Specifications	**F-3872**	**433-70**	**430-70**	**480-70**	**437-70**
Length, in (mm)	28 (711)	23 (584)	45 (1143)	45 (1143)	73 (1855)
Width, in (mm)	14.5 (368)	14 (355)	14.5 (368)	14.4 (366)	14.5 (368)
Weight, lbs. (kg)	2.8 (1.3)	2.9 (1.3)	3.9 (1.8)	3.9 (1.8)	5.5 (2.5)
Rated Wind Velocity, No Ice, mph (km/h)	160 (257)	160 (257)	150 (241)	150 (241)	150 (241)
Rated Wind Velocity, 0.5" (13mm) ice, mph (km/h)	120 (193)	120 (193)	110 (177)	110 (177)	110 (177)
Lateral Thrust @ 100 mph, wind, lbs. (kg)	9 (4.1)	8.7 (4.0)	16 (7.3)	15 (6.8)	25.8 (11.7)
Projected Area, ft² (m²)	0.34 (0.03)	0.32 (0.03)	0.61 (0.06)	0.55 (0.05)	0.96 (0.089)
Mounting Hardware Included	127-85 Clamp				

COMPROD Simplifying RF Solutions

sales@comprodcom.com | comprodcom.com
☎ US 1.877.825.2007 / CAN 1.800.603.1454
FAX 1.800.554.1033

Figure A.4. Receiver antenna data sheet. Source: [19] (page 1).

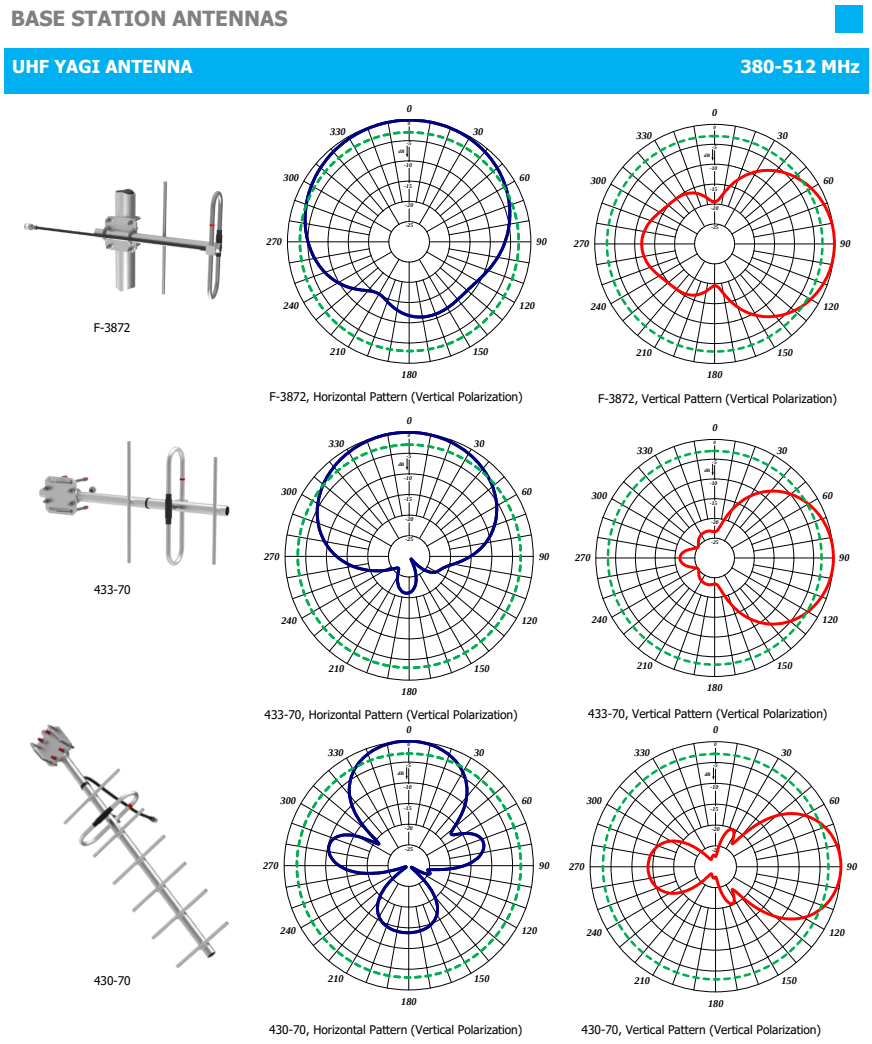

Figure A.4. Receiver antenna data sheet. Source: [19] (page 2).

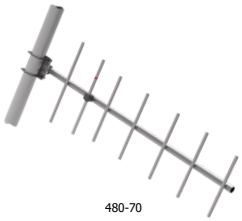

480-70

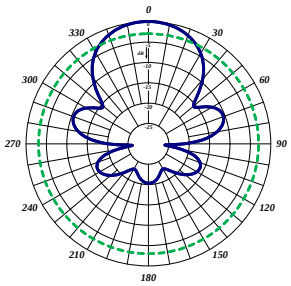

480-70, Horizontal Pattern (Vertical Polarization)

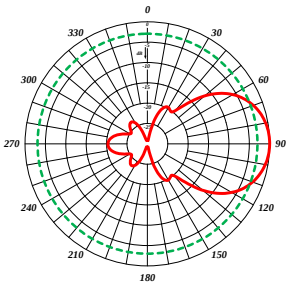

480-70, Vertical Pattern (Vertical Polarization)

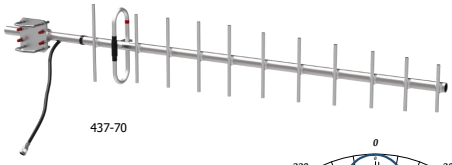

437-70

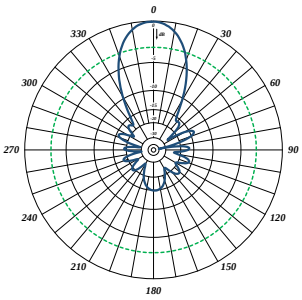

437-70, Horizontal Pattern (Vertical Polarization)

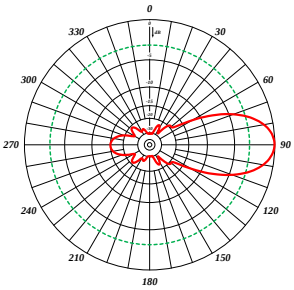

437-70, Vertical Pattern (Vertical Polarization)

COMPROD Simplifying RF Solutions

sales@comprodcom.com | comprodcom.com
US 1.877.825.2007 / CAN 1.800.603.1454
FAX 1.800.554.1033

Figure A.4. Receiver antenna data sheet. Source: [19] (page 3).

A.5 Pictures

Figure A.5. Setup for experiments 1-3: receiver antenna at 0° inclination

Figure A.6. Setup for experiments 4-6: receiver antenna at 24° inclination

Figure A.7. Setup for experiments 4-6: receiver antenna at 24° inclination page 2

Figure A.8. Setup for experiments 4-6: receiver antenna at 24° inclination page 3

Figure A.9. LT Negron, piloting the drone during take off

Figure A.10. LT Negron, piloting the drone during landing

Figure A.11. Professor Romero (left) and LT Negron (right) discussing controls

List of References

[1] J. Diao, M. Hedayati, and Y. E. Wang, "Experimental demonstration of distributed beamforming on two flying mini-drones," in *2019 United States National Committee of URSI National Radio Science Meeting (USNC-URSI NRSM)*, 2019, pp. 1–2.

[2] Y. Shi, R. Enami, J. Wensowitch, and J. Camp, "Measurement-based characterization of LOS and NLOS drone-to-ground channels," in *2018 IEEE Wireless Communications and Networking Conference (WCNC)*, 2018, pp. 1–6.

[3] S. Dill, E. Schreiber, M. Engel, A. Heinzel, and M. Peichl, "A drone carried multichannel synthetic aperture radar for advanced buried object detection," in *2019 IEEE Radar Conference (RadarConf)*, 2019, pp. 1–6.

[4] I. G. Cumming and F. H. Wong, *Digital processing of synthetic aperture radar data: Algorithms and implementation.* Boston: Artech House, 2005.

[5] A. R. C. B. Paul and D. W. Bliss, "Survey of RF communications and sensing convergence research," *IEEE Access*, vol. 5, pp. 252–270, 2017.

[6] A. L. J. R. Guerci, R. M. Guerci and D. Moskowitz, "Joint design and operation of shared spectrum access for radar and communications," *IEEE Radar Conf.*, pp. 1–6, May 2015.

[7] H. G. et al., "Radar spectrum engineering and management: Technical and regulatory issues," *Proc. IEEE*, vol. 103, no. 1, Jan, pp. 85–102, 2015.

[8] P. Y. S. D. Blunt and J. Stiles, "Intrapulse radar-embedded communications," *IEEE Trans. Aerosp. Electron. Syst.*, vol. 46, no. 3, pp. 1185–1200, 2010.

[9] M. L. Parmentar and R. A. Romero, "Opportunistic techniques to inject OFDM subcarriers into navigational radar spectral guard bands and mainlobe for spectrum sharing," *IEEE Radar Conf.*, pp. 1–6, Apr 2019.

[10] C. S. J. G. Metcalf and S. D. Blunt, "Impact of adjacent/overlapping communications waveform design within a radar spectrum sharing context," *IEEE Radar Conf.*, pp. 1–6, Apr 2020.

[11] Z. S. G. Meager, R. A. Romero, "Estimation and cancellation of high powered radar interference for communications signal collection," *IEEE Radar Conf.*, pp. 1–4, May 2016.

[12] C. Liu and R. Romero, "Radar-embedded communications MPSK demodulation with deep neural networks," *2020 European Radar Conference*, Jan 2021.

[13] J. C. Rohde and R. A. Romero, "Detection performance of embedded QPSK onto LFM waveform guard bands for RF convergence," *2021 IEEE Radar Conference*, pp. 1–6, 2021 [Online]. doi: 10.1109/RadarConf2147009.2021.9455227.

[14] M. A. Richards, *Fundamentals of radar signal processing*. New York: McGraw-Hill, 2014.

[15] NASA, "Get to know SAR/overview," 2022, accessed January 24, 2022, https://nisar.jpl.nasa.gov/mission/get-to-know-sar/overview/.

[16] Freefly Systems Inc., "Alta 8 specifications - dimensions," 2011, accessed January 12, 2022, https://freeflysystems.com/alta-8/specs.

[17] Vaunix Technology Corporation, "LMS-152D 250 – 1500 MHz (L-Band) USB programmable signal generator," 2021, accessed January 12, 2022, https://vaunix.com/lms-152d-digital-signal-generator/.

[18] Pasternack Enterprises Inc., "Product ID: PE51148," 2021, accessed January 12, 2022, https://www.pasternack.com/single-antenna-450-470-mhz-0-dbi-gain-sma-pe51148-p.aspx/.

[19] Comprod Inc., "430-70 UHF Yagi antenna," 2019, accessed January 12, 2022, https://https://comprodcom.com/shop/antennas-clamps/yagi-antennas/uhf-yagi-antenna-430-70/.

[20] Altair Inc., "Altair FEKO applications," 2022, accessed January 24, 2022, https://www.altair.com/feko-applications/.

Initial Distribution List

1. Defense Technical Information Center
   Ft. Belvoir, Virginia

2. Dudley Knox Library
   Naval Postgraduate School
   Monterey, California